MODEL-BASED ROBUST AND ADAPTIVE CONTROL OF TRANSFEMORAL PROSTHESES: THEORY, SIMULATION, AND EXPERIMENTS

A Thesis
Presented to
The Academic Faculty

By

Vahid Azimi

In Partial Fulfillment
of the Requirements for the Degree
Master of Science in the
School of Electrical and Computer Engineering

Georgia Institute of Technology

May 2020

MODEL-BASED ROBUST AND ADAPTIVE CONTROL OF TRANSFEMORAL PROSTHESES: THEORY, SIMULATION, AND EXPERIMENTS

Approved by:

Dr. Seth Hutchinson, Advisor
School of Interactive Computing
Georgia Institute of Technology

Dr. Dan Simon, Co-advisor
Department of Electrical Engineering and Computer Science
Cleveland State University

Dr. Chaouki T. Abdallah
School of Electrical and Computer Engineering
Georgia Institute of Technology

Dr. Aaron Young
School of Mechanical Engineering
Georgia Institute of Technology

Date Approved: January 27, 2020

To my parents.

ACKNOWLEDGEMENTS

I would like to thank my advisors, Profs. Seth Hutchinson, Dan Simon, and Aaron Ames for guiding and supporting me in this research. I would like to thank my thesis committee members for their helpful comments and suggestions. I would also like to thank my fellow graduate students and collaborators who contributed to this research.

This work was supported by the NSF under Award NRI-1526519 and Grant 1344954. This research was approved by the Georgia Institute of Technology and the California Institute of Technology Institutional Review Boards, protocol numbers H15255 and 16-0693, for testing with humans. The content of this thesis is IEEE-copyrighted, and was published in the *IEEE Transactions on Systems, Man and Cybernetics: Systems* and the *American Control Conference*.

TABLE OF CONTENTS

LIST OF TABLES

LIST OF FIGURES

SUMMARY

This thesis presents and experimentally implements five different robust, adaptive, and robust adaptive controllers as the first steps towards using model-based controllers for transfemoral prostheses. The goal of this research is to translate these control methods to the robotic domain, from bipedal robotic walking to prosthesis walking, including a rigorous stability analysis. The human/prosthesis system is first modeled as a two-domain hybrid asymmetric system. The model upon which the controllers are based is a 5-link planar hybrid system (both continuous and discrete behaviors) with point feet, to represent a transfemoral amputee's body and limbs. An optimization problem is formulated to obtain a stable human-like gait. The proposed controllers are then developed for the combined human/prosthesis model and the optimized reference gait. The stability of all five controllers is proven using the Lyapunov stability theorem and Barbalat's lemma, ensuring convergence to the desired gait. The proposed controllers are first verified on a bipedal walking robot as a hybrid human/prosthesis model in simulation. Simulations show that the proposed controllers are capable of meeting specific performance requirements regarding trajectory tracking of the prosthetic knee, convergence to a stable periodic orbit, and robustness to force/obstacle disturbances while walking on flat ground. They are then experimentally tested on a treadmill with an able-bodied subject using AMPRO3 (the third iteration of Advanced Mechanical Prosthesis), a custom self-contained powered transfemoral prosthesis. Results show that all controllers provide humanlike walking and accurate tracking performance for a healthy human subject utilizing a transfemoral prosthesis. Finally, outdoor tests are carried out using AMPRO3 with three test subjects walking on level ground, uphill slopes, and downhill slopes at slope angles of 3° and 8°, to demonstrate walking in different real-world environments.

CHAPTER 1
INTRODUCTION

The number of transfemoral amputees in the United States is at around 222,000 [1]. Persons with amputation can utilize prosthetic legs to reestablish typical activities of daily living. There are three general types of prosthetic legs: passive, active, and semi-active [2, 3]. Among them, active prostheses enable amputees to walk with a more natural gait compared with the other types while simultaneously allowing the users to walk more efficiently at different speeds with less fatigue [4]. Motivated by the large number of above-knee amputations and advantages of active prostheses, researchers have recently concentrated on design and control of powered prostheses [5, 6].

In this thesis, five model-based controllers are formulated for powered transfemoral prostheses as a means of addressing limitations of model-free control approaches such as variable impedance (VI) and proportional-derivative (PD) controllers. The objective is to guarantee convergence/boundedness of system solutions in the presence of modeling error and disturbances through a rigorous systematic stability analysis. All proposed controllers are first implemented on a 5-link planar walking biped model in simulation and then experimentally tested using AMPRO3, which is shown in Fig. 1.1. Simulations show that the proposed controllers effectively meet performance requirements such as tracking and robustness to force/obstacle disturbances. Treadmill test results show that all proposed controllers provide humanlike walking and good prosthesis knee tracking. A comprehensive comparison is then performed during the treadmill test to show superiority of the proposed model-based controllers over the VI and PD controllers. The outdoor test is performed with three test subjects as shown in Fig. 1.1 walking on level ground, uphill slopes, and downhill slopes at slope angles of 3° and 8°. Outdoor test results show that the proposed controllers provide convergence of the system trajectories to a stable limiting periodic orbit, resulting in stable walking using AMPRO3 on all tested terrains.

Subject #1 Subject #2 Subject #3

Figure 1.1: Outdoor test with three healthy test subjects wearing the powered transfemoral prosthesis, AMPRO3

1.1 Background

At present, model independent VI control is the most common approach for controlling active prosthetic legs [7, 8]. However, impedance control suffers several shortcomings: tedious impedance parameter tuning (unique to each specific amputee subject), difficulties in determining sub-phase thresholds, lack of feedback, and passiveness [7, 9]. To address some of the limitations of ordinary impedance control, a prosthetic impedance controller combining a control Lyapunov function (CLF) with model independent quadratic programs (MIQP) was recently developed [10, 11]. In those papers, the proposed controller was tested on the planar 5-link bipedal robot AMBER (Advanced Mechanical Bipedal Experimental Robot) and AMPRO (AMBER Prosthesis), a self-contained powered transfemoral prosthesis, both in simulation and experiment. The authors achieved better tracking performance and improved energy efficiency compared to VI control. To address the tuning problem of the VI controllers, automatic tuning approaches have been recently used for

control of a powered prosthetic leg [12]. However, since the above-mentioned controllers were designed in a model-free fashion, the formal stability analysis of the controllers was not provided.

The PD control paradigm is another popular approach in robotics applications. With this paradigm, gravitational effects are unknown, and this type of controller yields steady state tracking error. Since perfect knowledge of the system dynamics is rarely available, the VI and PD controllers are designed independently of model information, involving only the tracking error in their structures (called model-free controllers). As a consequence, these approaches do not take into account model information and are not able to include model uncertainty in the stability analysis. In other words, although model-free controllers are able to provide reasonable control performance, a formal proof is hard to derive. Thus, the aforementioned controllers lack a formal guarantee of stability and robustness in the presence of system uncertainties, unmodeled dynamics, and disturbances. However, these influences may degrade the performance of the closed-loop system or even lead to instability. A rigorous systematic stability analysis is required to guarantee convergence/boundedness of the system in the presence of unknown model uncertainties and external disturbances. Through this stability analysis, convergence of error trajectories is formally guaranteed in the presence of unknown system information about user and prosthesis dynamics. This analysis can be provided only by using model-based controllers to guarantee the control objectives for different users, different prostheses, and in the presence of unknown bounded model errors and disturbances.

There have been a few attempts to analyze the stability of VI control in robotics applications. In [13], a tank-based approach to impedance control with variable stiffness is proposed based on the total energy of the manipulator. In that approach, the stiffness profile is state-dependent and modified online. Its performance is heavily dependent on the initial and threshold levels of energy in the tank. These shortcomings make this method sensitive to perturbations and prone to instability. As an improvement to the state-dependent tank-based approach, stability considerations for variable impedance control are proposed in [14]. That work provides a stability condition for varying stiffness and damping that is state independent and can be found offline. However, that

method requires model knowledge, dynamic decoupling, and measurement of external effort in interaction tasks.

Several results of model-based controllers have recently been attained on robot manipulators, prostheses, humanoid robots, and servo systems [15, 16, 17, 18, 19]. In [17], an active disturbance rejection adaptive controller was designed for a class of nonlinear systems with modeling uncertainty. Both parametric uncertainties and uncertain nonlinearities were estimated and then compensated in a feedforward way. The motion control of a motor-driven robot manipulator was investigated to verify the tracking performance of the control strategy. In [18], an adaptive integral robust controller was designed for a class of uncertain nonlinear systems. To ensure robustness against disturbances, the controller gain was updated online without prior bound knowledge of the disturbances. An electromechanical servo system driven by a motor was considered to verify the effectiveness of the proposed controller. In [19], four robust model reference adaptive impedance observer/controller combinations were designed for ground reaction force (GRF) estimation-based control of a prosthesis and a legged robot model. These approaches were designed to control the system while compensating for the GRF effects, parametric uncertainties, and unmodeled dynamics.

1.2 Contributions

Motivated by the aforementioned shortcomings, this thesis is the first step towards designing model-based adaptive and robust adaptive control for prosthetic walking. Stability and robustness of the proposed controllers are formally guaranteed in the presence of model uncertainties and disturbances such as unforeseen forces and obstacles.

The important contributions of this work are: (i) Formulation of robust, adaptive, and robust adaptive controllers for bipedal robotic walking (human/prosthesis system) with formal stability and robustness analyses, (ii) Evaluation of tracking performance and force/obstacle disturbance robustness on the walking biped platform as shown in Fig. 1.2, (iii) Experimental verification with treadmill walking by an able-bodied subject of the proposed controllers of the powered trans-

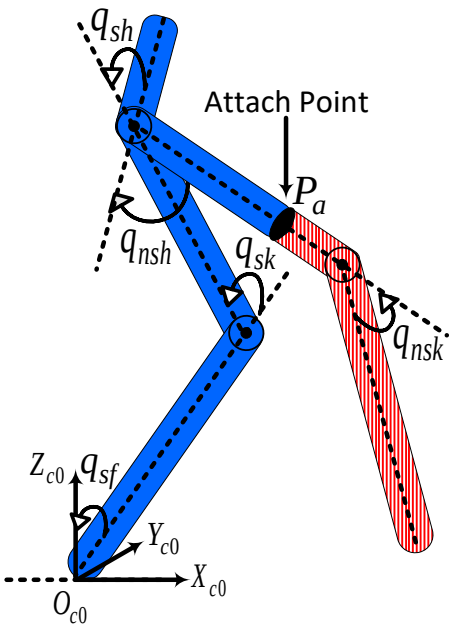

Figure 1.2: The 5-link planar model with point prosthetic foot, where the red cross-hatched part represents the prosthesis.

femoral prosthesis AMPRO3 (the third iteration of AMPRO) as shown in Fig. 1.1, (iv) Experimental demonstration with treadmill walking of the superiority of the proposed model-based controllers compared to the VI and PD controllers with regard to tracking performance and torque optimality, and (v) Experimental outdoor demonstration of AMPRO3 with the proposed controllers by three test subjects on level ground, uphill slopes, and downhill slopes, for slope angles of 3° and 8° as shown in Fig. 1.1.

To begin, an active transfemoral prosthesis is first modeled with the prismatic-prismatic-revolute-revolute (PPRR) joint structure. The human/prosthesis system is then modeled using a point prosthetic foot 5-link planar hybrid model comprised of one torso, two thighs, and two shanks. Using able-bodied reference trajectories, an optimal smooth humanlike gait is found by solving an optimization problem. For the human/prosthesis system and the generated gait, five different model-based controllers are designed: the pure adaptive controller (ADC), the robust sliding mode adaptive controller (RSAC), the adaptive integral controller (AIC), the robust sliding mode controller (RSC), and the robust passivity-based controller (RPC). The stability of all proposed controllers

is proven using the Lyapunov stability theorem and Barbalat's lemma for continuous dynamics of the prosthesis system.

The proposed robust controllers, RSC and RPC, are designed with the aim of achieving robustness to parametric uncertainties, unmodeled dynamics, and disturbances of the human-prosthesis system while providing good tracking. Relying on the learning and adaptation nature of adaptive controllers, the ADC is designed to estimate unknown prosthetic leg parameters and user mass in order to achieve good tracking performance. To take one step further towards enhancing tracking performance, the AIC is designed using a time-varying sliding surface exploiting the integral of position error. However, the ADC and AIC only investigate parametric uncertainties while ignoring unmodeled dynamics and disturbances. The aforementioned advantages of adaptive control along with the presence of both disturbances and nonparametric uncertainties motivates the blending of ADC and RSC to construct the RSAC. The RSAC can provide robustness to all parametric and non-parametric uncertainties, and provide convergence of error trajectories of the system to a boundary layer. This robustness is maintained while the unknown parametric uncertainty of the system is identified by an adaptation mechanism. The proposed RSAC can achieve the same control objectives as [17, 18, 19], but with a simpler and more straightforward design procedure.

Model-free neural-network (NN)-based adaptive controllers can also be employed for robust adaptive control. These controllers can be used to eliminate the need for the knowledge of the dynamic model structure [20, 21, 22, 23]. However, such controllers require a more complicated control structure and incur more computational cost compared to model-based adaptive controllers. Because the modeling of the prosthesis device (Chapter 2.2) is a straightforward task, there is no need to choose the NN-based adaptive controller, and a simpler control structure such as the model-based controllers proposed here are preferred.

The goal is to translate the proposed methods to the robotic domain, taking inspiration from bipedal locomotion. The proposed controllers in this thesis are first verified in simulation on a walking biped platform and then compared with each other with respect to robustness and tracking performance. Simulation results illustrate that all five proposed systems have good tracking perfor-

mance and robustness, qualitatively emulating humanlike walking. All five proposed controllers are then experimentally verified on AMPRO3 with the human test subject walking for 2.5 min at a treadmill speed of 2 mph, achieving good tracking and reasonable prosthesis knee torque values. Treadmill test results also show that the proposed model-based controllers outperform the VI and PD controllers with regard to tracking performance and torque requirements. In addition to the treadmill test, outdoor tests are performed using AMPRO3 with three test subjects (as shown in Fig. 1.1) walking on different outdoor terrains: level ground, uphill, and downhill at slope angles of 3° and 8°. Outdoor tests reveal that the proposed controllers provide stable periodic walking not only on level ground but also on uneven surfaces. Our experiments and simulations can be seen in a video [24].

The thesis is organized as follows: Chapter 2 describes the combined human/prosthesis system and presents the problem statement. Chapter 3 presents the proposed controller structures along with their stability analyses. Chapter 4 presents simulation results for tracking performance and robustness to disturbances. Chapter 5 presents experimental results on AMPRO3. Chapter 6 presents discussion, concluding remarks, and future work.

CHAPTER 2

HUMAN/PROSTHESIS SYSTEM AND PROBLEM STATEMENT

A human/prosthesis system can be modeled as a walking biped. It is, therefore, reasonable to adopt bipedal robots as a platform to test the prosthesis controllers. In this section, modeling and control of a 5-link planar walking biped (one torso, two thighs, and two shanks) shown in Fig. 1.2 is first studied. The prosthetic device is then modeled using a PPRR joint structure for the prosthesis control formulation. Finally, problem statement and proposed control architecture are explained.

2.1 Modeling and Control

A walking biped (i.e., a system with impulse effects) can be modeled as a hybrid system consisting of a sequence of continuous (leg swinging forward) and discrete (impact at foot strike) events. The human/prosthesis walking structure can be defined with configuration space Q_R in local coordinates $q_c = (q_{sf}, q_{sk}, q_{sh}, q_{nsh}, q_{nsk})^T$ with world frame $O_{co} = \{x_{co}, y_{co}, z_{co}\}$ as illustrated in Fig. 1.2. The formal definition of hybrid systems can be found in [25, 26]. As shown in Fig. 1.2, q_{sf} is the angle of the stance foot, q_{sk} is the angle of the stance knee, q_{sh} is the angle of the stance hip, q_{nsh} is the angle of the non-stance hip, and q_{nsk} is the angle of the non-stance knee. Using the Euler-Lagrange formula [27], the equations of motion of the bipedal continuous dynamics are given as

$$M_c(q_c)\ddot{q}_c + C_c(q_c, \dot{q}_c)\dot{q}_c + g_c(q_c) = Bu_c, \tag{2.1}$$

where $M_c(q_c) \in \Re^{5\times5}$ is the inertia matrix; $C_c(q_c, \dot{q}_c) \in \Re^{5\times5}$ is the Coriolis and centripetal matrix; $g_c(q_c) \in \Re^{5\times1}$ is the gravity vector; $B \in \Re^{5\times5}$ is the torque map with underactuated prosthesis side and actuated human side; $u_c \in \Re^{5\times1}$ is the vector of torque inputs.

When the non-stance foot hits the ground, angular velocities of the human-prosthesis bipedal model change upon impact while the stance and non-stance legs are switched. The discrete dy-

namics of the biped can therefore be considered as the impact dynamics, which are derived based on the holonomic constraints applied for the subsequent domain [26]. To consider impulse effects of the combined system right before and after impact, a reset map with the assumption of perfect plastic impact [28] is presented as [29]

$$\triangle_r\ (q_c, \dot{q}_c) = \begin{bmatrix} \triangle_{q_c}\ q_c \\ \triangle_{\dot{q}_c}(q_c)\dot{q}_c \end{bmatrix}, \tag{2.2}$$

where $\triangle_{q_c}$ relabels and switches the stance and nonstance leg at impact and $\triangle_{\dot{q}_c}$ gives the velocity change due to impact.

To emulate humanlike walking, actual combined system outputs y_a must converge to desired human outputs y_d. The desired human outputs $y_d(t, \xi)$ (a function of time and parameter set ξ) for walking and running can be defined as the time solution to a linear mass-spring-damper system by the canonical walking function (CWF) [30]:

$$y_d(t, \xi) = e^{-\xi_1 t}\left(\xi_2 \cos(\xi_3 t) + \xi_4 \sin(\xi_3 t)\right) + \xi_5, \tag{2.3}$$

where the relation between the CWF of Eq. 2.3 and the solution to a linear mass-spring-damper system reveals that $\xi_1 = \xi_d \omega_n$ with ξ_d as the damping ratio and ω_n as the natural frequency; $\xi_5 = g$ is the gravity and $\xi_3 = \omega_n$; and ξ_2 and ξ_4 are determined by the initial conditions of the system. Note that the number of the parameters is $N_\xi = 5$.

Therefore, convergence of the actual human outputs $y_a(q_c, \dot{q}_c)$ (function of the biped's states) to the desired human outputs $y_d(t, \xi)$ of Eq. 2.3 implies convergence of their difference to zero. In other words, the human-inspired controller can be applied to drive the following outputs to zero:

$$y(q_c, \dot{q}_c, \xi) = y_a(q_c, \dot{q}_c) - y_d(t, \xi), \tag{2.4}$$

where $y(q_c, \dot{q}_c, \xi)$ is comprised of relative degree one and relative degree two virtual constraints. For the point prosthetic foot 5-link planar model in this work, the actual outputs y_a are com-

prised of forward hip velocity (v_{hip_x}), stance knee angle (ska), non-stance knee angle $(nska)$, non-stance leg slope $(nsls)$, and torso angle (ta) [31]. Note that forward hip velocity is the relative degree one output, which is a function of both biped position and velocity $(y_{a1}(q_c, \dot{q}_c))$, and the other outputs are considered relative degree two outputs, which are only a function of biped configuration variables $(y_{a2}(q_c))$. Thus, the number of the relative degree one and two outputs respectively are $N_{y_{a1}} = 1$ and $N_{y_{a2}} = 4$. Also, note that the parameters of all of the outputs is $\xi = (v_{hip_x}, \xi_{ska}, \xi_{nska}, \xi_{nsls}, \xi_{ta}) \in \Re^{(N_\xi \times N_{y_{a2}})+1}$, so the total number of parameters is $N_{\xi_t} = (N_\xi \times N_{y_{a2}}) + 1$.

Since forward hip velocity of the biped, which is the first actual output, is roughly constant during walking, its forward hip position can be approximated as $p_{hip_x} = v_{hip_x} t$ [32]. The constant forward hip velocity is an important attribute of human walking, and $t = p_{hip_x}/v_{hip_x}$. For the sake of time-invariance of the control structure, t in the time-based desired human output $y_d(t, \xi)$ of Eq. 2.3 can be replaced by the following parameterized time [25]:

$$\tau(q_c) = \frac{p_{hip_x}(q_c) - p_{hip_x}(q_c^0)}{v_{hip_x}}, \tag{2.5}$$

where p_{hip_x} is the forward hip position and $p_{hip_x}(q_c^0)$ denotes its initial value. Using this parametrization of time, the human-inspired outputs of Eq. 2.4 can be rewritten as

$$y(q_c, \dot{q}_c, \xi) = \begin{pmatrix} y_1(q_c, \dot{q}_c, \xi) \\ y_2(q_c, \xi) \end{pmatrix} = \begin{pmatrix} y_{a1}(q_c, \dot{q}_c) - v_{hip_x} \\ y_{a2}(q_c) - y_d(\tau(q_c), \xi) \end{pmatrix}, \tag{2.6}$$

where v_{hip_x} and $y_d(\tau(q_c), \xi)$ are state-based desired outputs for the relative degree one and relative degree two human outputs respectively.

Although the feedback linearization human-inspired controller drives the aforementioned human-inspired outputs to zero and provides exponential stability of the continuous dynamics, it is also essential to keep these outputs zero upon impact. While the relative degree one output (forward velocity) of a human is relatively constant during walking, relaxing the hip velocity constraint is desirable when impact occurs. Therefore, the following partial zero dynamics (PZD) surface is

only considered on the relative degree two output $y_2(q_c, \xi)$:

$$\mathscr{P}\mathscr{Z}_\xi = \{(q_c, \dot{q}_c) \in Q_R : y_2(q_c, \xi) = 0, \dot{y}_2(q_c, \xi) = 0\}. \tag{2.7}$$

To guarantee invariance of the reset map $\triangle_r$ of the PZD of each domain, the partial hybrid zero dynamics (PHZD) are introduced as [29, 33]

$$\text{PHZD} : \triangle_r(S_r \cap \mathscr{P}\mathscr{Z}_\xi) = \mathscr{P}\mathscr{Z}_\xi, \tag{PHZD}$$

where S_r denotes the switching surface of the biped model for transitions to the next domain.

Now, the goal is to find the set $\xi \in \Re^{(N_\xi \times N_{y_{a2}})+1}$ using an optimization problem subject to both PHZD and other physical constraints (foot clearance in addition to position and velocity joint limits), providing an optimal and stable human-like gait:

$$\begin{aligned} \xi^* = \underset{\xi \in \Re^{(N_\xi \times N_{y_{a2}})+1}}{\text{argmin}} \quad & \text{COST}(\xi) \\ \text{s.t. } & \text{PHZD } \& \text{ Physical Constraints,} \end{aligned} \tag{2.8}$$

where COST is a human data-based cost function, which is the least-squares-fit error between human walking data obtained from IMUs (inertial measurement units) and the CWF [30]. This function is defined as

$$\text{COST}(\xi) = \sum_{i=1}^{N_{y_2}} \sum_{j=1}^{N_p} \left[y_{a2_i}(q_c[j]) - y_{d_i}(t_i[j], \xi_i) \right]^2 + \sum_{j=1}^{N_p} \left[p_{hip_x}(q_c[j]) - (v_{hip_x} t[j] + p_{hip_x}(q_c[0])) \right]^2, \tag{2.9}$$

where $t[j]$ is the discrete time and N_p is the number of discrete time points.

The first part of COST calculates the set $(\xi_{ska}, \xi_{nska}, \xi_{nals}, \xi_{ta})$ by least squares fitting of the CWF and the human data of the relative degree two outputs. The second part determines the constant v_{hip_x} by minimizing the difference between the actual forward hip position and the linearized

one from Eq. 2.5. Thus, by solving this optimization problem, the set ξ^* can be found so that COST$(\xi^*) \leq \delta$ for some small positive constant δ. This implies that when the outputs of the walking biped follow the desired human outputs $y_d(t, \xi^*)$, the human/prosthesis system acts like a linear mass-spring-damper system. In this work, the optimization problem of Eq. 2.8 is performed by the MATLAB function *fmincon* to find the set $\xi \in \Re^{21}$.

It should be pointed out that when the parameter set ξ is optimized subject to PHZD constraints, tracking invariance of the relative degree two outputs is guaranteed even at impact. This provides smooth transitions between stance and non-stance phases. With desired human-inspired outputs from the optimization problem of Eq. 2.8, desired joint angles and angular velocities of the combined system (q_c^d) are calculated via inverse projection from the PHZD surface using the PHZD reconstruction procedure [26].

2.2 Prosthesis Model

The prosthetic device (red portion in Fig. 1.2) can be modeled using a PPRR joint structure as illustrated in Fig. 2.1. The equations of motion of the prosthetic leg are:

$$M_p(q_p)\ddot{q}_p + C_p(q_p, \dot{q}_p)\dot{q}_p + g_p(q_p) = u_{p_i} + d_p(t), \tag{2.10}$$

where $q_p = (q_{p1}, q_{p2}, q_{p3}, q_{p4})^T$, q_{p1} and q_{p2} are the horizontal and vertical displacements of the attach point P_a respectively, and q_{p3} and q_{p4} are thigh and knee angles respectively; $M_p(q_p) \in \Re^{4\times4}$, $C_p(q_p, \dot{q}_p) \in \Re^{4\times4}$, and $g_p(q_p) \in \Re^{4\times1}$ are the inertia matrix, Coriolis and centripetal matrix, and gravity vector respectively; $u_{p_i} \in \Re^{4\times1}$ is the prosthesis control signal generated by the i^{th} controller (*i*=1,2,3) presented in Section 3, where u_{p_i} is comprised of horizontal and vertical forces at the hip and active control torques at the thigh and knee; and $d_p(t) \in \Re^{4\times1}$ is a time varying disturbance. Note that the prosthesis is attached to the amputee at P_a (the socket adapter) shown in Fig. 1.2 and the world frame for the prosthesis system is represented as $O_o = \{x_o, y_o, z_o\}$ shown in Fig. 2.1.

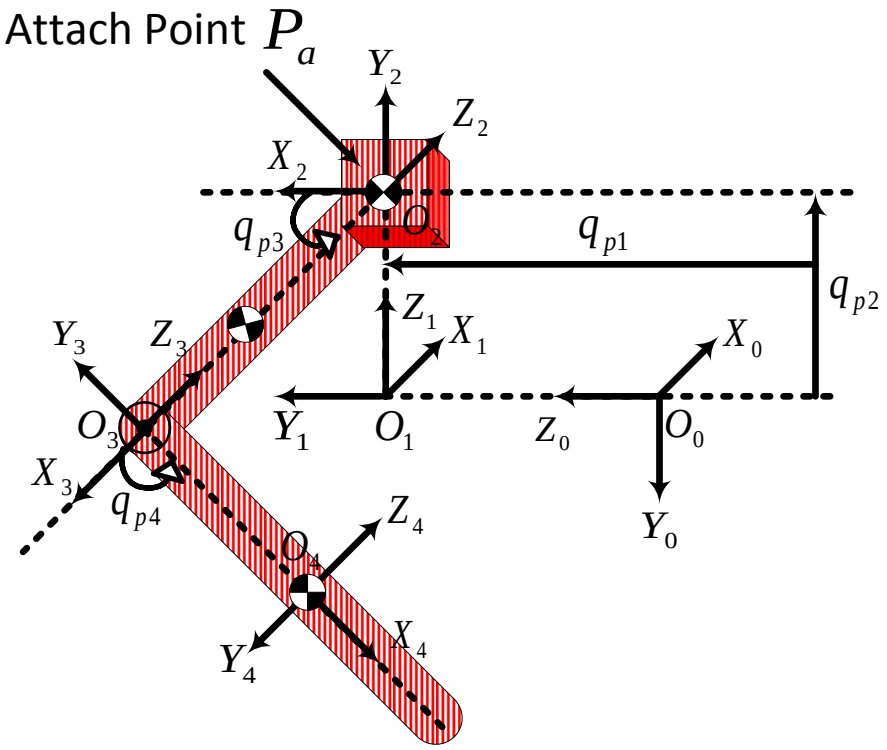

Figure 2.1: Transfemoral prosthesis model

The following properties of the model of Eq. 2.10 are used when developing the proposed algorithms.

Property 1: The inertia matrix $M_p(q_p)$ is symmetric, positive definite, and uniformly bounded.

Property 2: The matrix $\dot{M}_p(q_p) - 2C_p(q_p, \dot{q}_p)$ is skew-symmetric.

Property 3: The Coriolis and centripetal matrix $|C_p(q_p, \dot{q}_p)| \leq \kappa |\dot{q}_p|$ for $\kappa > 0$ and $|\dot{q}_p| \leq \dot{q}_{p_{max}}$ for each joint.

Property 4: The system dynamics of Eq. 2.10 can be linearly parameterized by a model regressor matrix $Y(q_p, \dot{q}_p, \ddot{q}_p) \in \Re^{n \times r}$ and a parameter vector $p \in \Re^{r \times 1}$ as

$$M_p(q_p)\ddot{q}_p + C_p(q_p, \dot{q}_p)\dot{q}_p + g_p(q_p) = Y(q_p, \dot{q}_p, \ddot{q}_p)p, \tag{2.11}$$

where r and n are the number of parameter vector elements and number of the joints respectively.

This prosthetic leg model has four degrees of freedom: horizontal and vertical displacements of

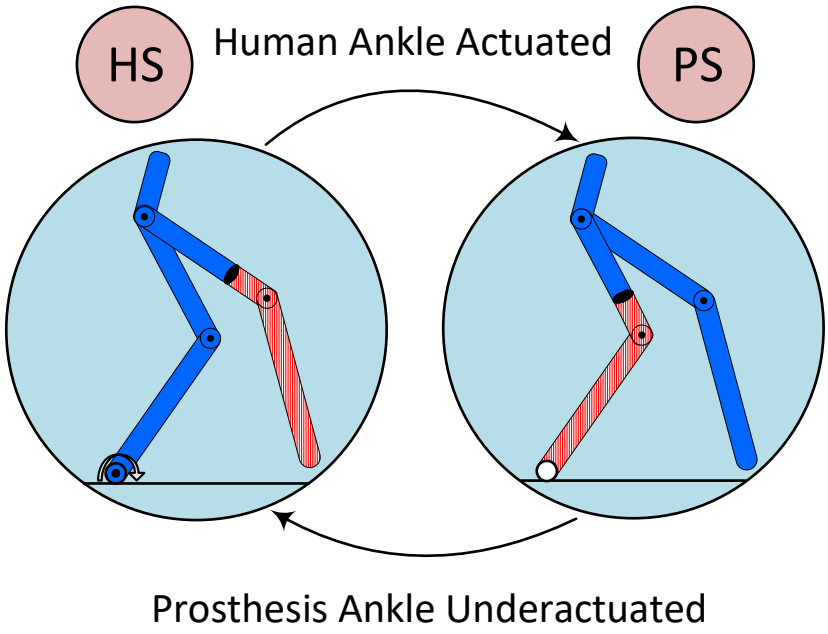

Figure 2.2: Two-domain hybrid asymmetric human-prosthesis system with actuated human ankle and underactuated prosthesis ankle

the attach point P_a, thigh angle, and knee angle. In this work, the prosthetic ankle is passive while the human one is obviously actuated, resulting in a two-domain hybrid asymmetric human/prosthesis system. Figure 2.2 shows this two-domain system with one domain for human stance (HS) and the other for prosthetic stance (PS).

2.3 Problem Statement

The scope of this thesis encompasses control of the prosthetic knee joint shown in Fig. 1.2 using the five proposed controllers introduced in Chapter 3. These model-based controllers are presented as a means of addressing the limitations of the VI and PD controllers. Using the proposed controllers, we formally present stability and robustness of the closed-loop system in the presence of system uncertainties and disturbances. We also greatly improve prosthesis knee tracking performance compared to the VI and PD controllers. We finally verify our controllers on AMPRO3 in an outdoor test with three subjects walking on different flat and uneven surfaces.

The proposed controllers use only $S_c = \{q_c, q_c^d\}$ and hip information from the human/prosthesis

Table 2.1: Linear transformation between hip information and coordinates of the healthy body in Fig. 1.2, and local degrees of freedom of the prosthesis model in Fig. 2.1

Stance phase	Swing phase
$q_{p1} = p_{hip_x}$	$q_{p1} = p_{hip_x}$
$q_{p2} = p_{hip_z} - L_z$	$q_{p2} = p_{hip_z} - L_z$
$q_{p3} = -q_{sk} + \pi/2$	$q_{p3} = -q_{sk} + q_{sh} - q_{nsh} + \pi/2$
$q_{p4} = q_{sk}$	$q_{p4} = q_{nsk}$

system without any information about the user and prosthesis dynamics. From S_c and using a linear transformation in Table 2.1, $S_p = \{q_p, q_p^d\}$ can be computed. In Table 2.1, q_p^d is the desired trajectory for q_p; p_{hip_x} and p_{hip_z} are horizontal and vertical positions of the hip; and L_z denotes vertical distance between the world frames O_{c0} and O_0. The set S_p is then used by the controllers to generate prosthetic knee torque u_p during both swing and stance phases, allowing the combined human-prosthesis system to emulate humanlike walking, i.e., $q_p \to q_p^d \Rightarrow q_c \to q_c^d \Rightarrow y_a \to y_d$.

Since body coordinates are defined based on stance and non-stance phases, the fourth element of u_p is replaced by the second element of u_c when the prosthesis device is the stance leg, and likewise, the fourth element of u_p is replaced by the fifth element of u_c when the prosthesis is the non-stance leg (the first three elements of the u_p are dummy and not used). In this manner, the prosthesis control signal remains correctly defined during stance and non-stance phases. Our controllers use only body coordinates and able-bodied reference trajectories of the combined system, without any dynamic information of the healthy body, to generate prosthetic knee torque, which allows the combined human-prosthesis system to emulate humanlike walking. This implies that the proposed controllers are robust against different amputee subjects. See Fig. 2.3 for the proposed control architecture.

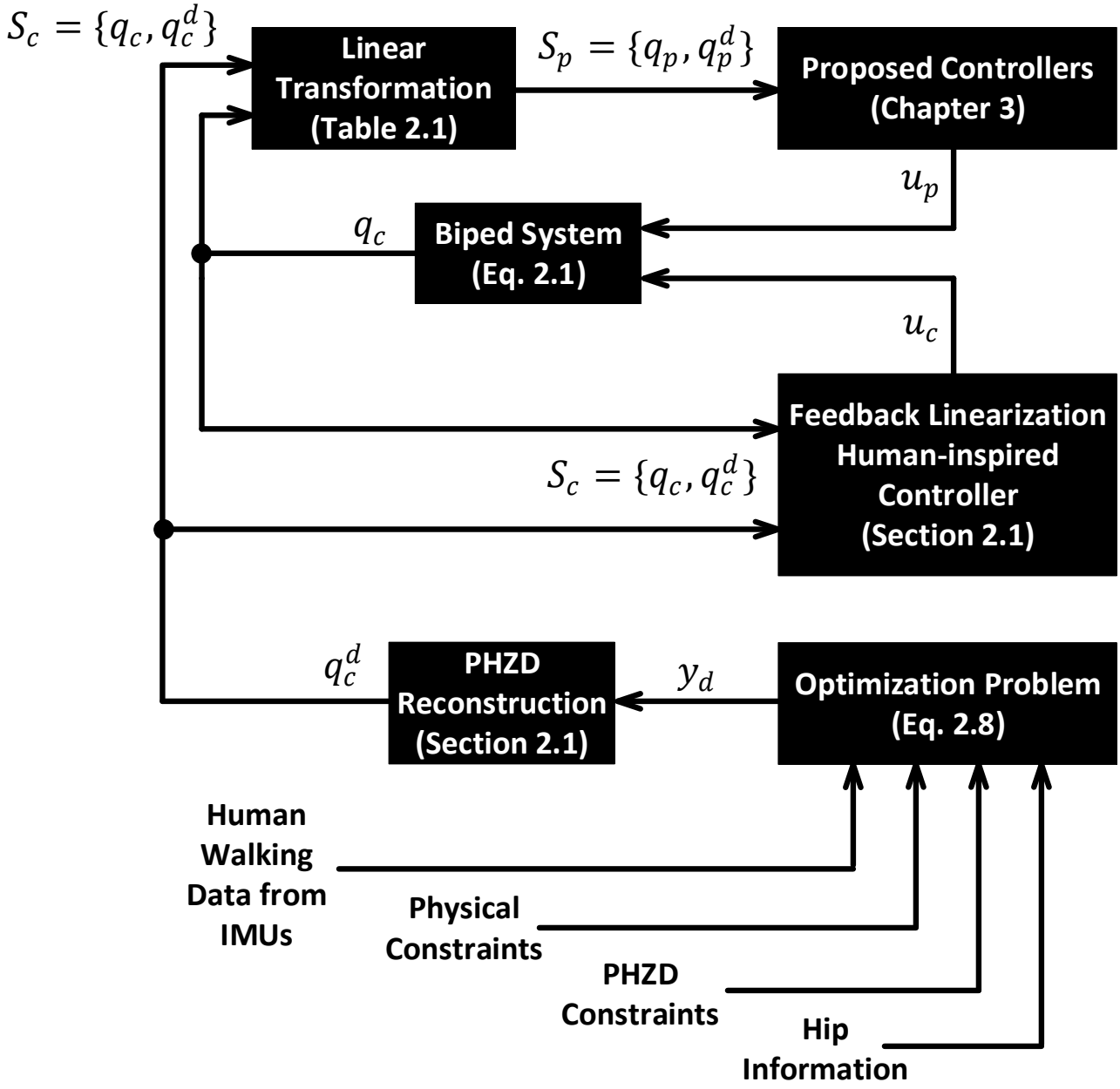

Figure 2.3: Proposed structure for the biped system

CHAPTER 3

PROPOSED PROSTHESIS CONTROLLERS

This section presents five different model-based controllers, ADC, RSAC, AIC, RSC, and RPC to control the prosthetic knee joint while the other joints are controlled by a feedback linearization human-inspired controller [26]. As all controllers are model-based, the prosthesis model depicted in Fig. 2.1 is used to control the prosthetic knee joint (red part) shown in Fig. 1.2. In practice, all joints are controlled by the amputee other than the active prosthetic knee. This framework results in convergence of the outputs of the human/prosthesis system y_a to the desired ones y_d exponentially and provides stable and humanlike walking.

3.1 Adaptive Controller (ADC)

Robustness to only parametric uncertainties, no unmodeled dynamics, and zero disturbances.

Adaptive control implements learning and adaptation using online parameter vector ($p \in \Re^{r\times 1}$) estimation in the control structure. The ADC aims to enhance tracking performance using estimation of the unknown prosthetic leg parameters while not considering unmodeled dynamics or disturbances ($d_p(t) = 0$). In this section, a direct adaptive controller, which is a combination of a PD controller and tracking-error-based (TEB) adaptation mechanism, is presented [34].

Given Property 4, the system dynamics of Eq. 2.10 can be linearly parameterized as

$$M_p(q_p)\ddot{q}_p + C_p(q_p, \dot{q}_p)\dot{q}_p + g_p(q_p) = Y(q_p, \dot{q}_p, \ddot{q}_p)p. \tag{3.1}$$

Defining an error vector $s = \dot{e} + \lambda e$ and signal vector $v = \dot{q}_p^d - \lambda e$, the ADC control law can be expressed as [35, 36]:

$$u_{p_{\text{ADC}}} = Y(q_p, \dot{q}_p, v, \dot{v})\hat{p} - K_{d_{\text{ADC}}}s, \tag{3.2}$$

where $e = q_p - q_p^d$ and $\lambda = \text{diag}(\lambda_1, \lambda_2, ..., \lambda_n), \lambda_i > 0$; $K_{d_{\text{ADC}}}$ is a diagonal matrix with positive elements; $Y(q_p, \dot{q}_p, v, \dot{v})$ is the acceleration-free version of $Y(q_p, \dot{q}_p, \ddot{q}_p)$ [37]; and $\hat{p}$ is adjusted based on system joint measurements and the adaptation mechanism. Substituting Eq. 3.2 into Eq. 2.10 in the absence of non-parametric uncertainties and other disturbances, we have the closed-loop system

$$M_p(q_p)\dot{s} + C_p(q_p, \dot{q}_p)s + K_{d_{\text{ADC}}}s = Y(q_p, \dot{q}_p, v, \dot{v})\tilde{p}, \tag{3.3}$$

where $\tilde{p}$ is the parameter vector estimation error.

Consider the Lyapunov function candidate [35]:

$$V_{\text{ADC}}(s, \tilde{p}) = \frac{1}{2}\left(s^T M_p(q_p)s + \tilde{p}^T\gamma\tilde{p}\right), \tag{3.4}$$

where V_{ADC} is a function of s and $\tilde{p}$, and γ is a design parameter such that $\gamma = \text{diag}(\gamma_1, \gamma_2, ..., \gamma_r), \gamma_i > 0$.

Theorem 1: *Given the Lyapunov function $V_{ADC}(s, \tilde{p})$ of Eq. 3.4, and the ADC control law of Eq. 3.2 in conjunction with the adaptation law $\dot{\hat{p}}_1 = -\gamma^{-1}Y^T(q_p, \dot{q}_p, v, \dot{v})s$, we obtain $\dot{V}_{ADC}(s, \tilde{p}) \to 0$ as $t \to \infty$, which implies asymptotic stability of the closed-loop system, implying $s \to 0$ and $q_p \to q_p^d$ for all $\tilde{p} \in \Re^r$.*

Barbalat's Lemma [35] is used to prove Theorem 1.

Barbalat's Lemma (first version): If a candidate Lyapunov function $V(t, x)$ satisfies the conditions: (i) $V(t, x)$ is lower-bounded, (ii) $\dot{V}(t, x)$ is negative semi-definite, and (iii) $\ddot{V}(t, x)$ is bounded, then $\dot{V}(t, x) \to 0$ as $t \to 0$.

Proof of Theorem 1: Taking the time derivative of Eq. 3.4, substituting the closed-loop system of Eq. 3.3, and using Property 2 $\left(s^T(\dot{M}_p(q_p) - 2C_p(q_p, \dot{q}_p))s = 0\right)$ yields

$$\dot{V}_{\text{ADC}}(s, \tilde{p}) = -s^T K_{d_{\text{ADC}}}s + s^T Y(q_p, \dot{q}_p, v, \dot{v})\tilde{p} + \dot{\tilde{p}}^T\gamma\tilde{p}. \tag{3.5}$$

The adaptation law $\dot{\hat{p}}_1 = -\gamma Y^T(q_p, \dot{q}_p, v, \dot{v})s$ yields

$$\dot{V}_{\text{ADC}}(s, \tilde{p}) = -s^T K_{d_{\text{ADC}}} s. \tag{3.6}$$

Since $\dot{V}_{\text{ADC}}(s, \tilde{p})$ of Eq. 3.6 is negative semi-definite, using Barbalat's Lemma [35] it can be shown that $\dot{V}_{\text{ADC}}(s, \tilde{p}) \to 0$. Since $V_{\text{ADC}}(s, \tilde{p})$ of Eq. 3.4 is lower-bounded and Eq. 3.6 implies $V_{\text{ADC}}(t) \leq V(0)$, $V_{\text{ADC}}(s, \tilde{p})$ and in turn s and $\hat{p}$ are bounded. To check if $\dot{V}_{\text{ADC}}(s, \tilde{p})$ is uniformly continuous in time, the second derivative of Eq. 3.6 is calculated as

$$\ddot{V}_{\text{ADC}}(s, \tilde{p}) = -s^T K_{d_{\text{ADC}}} \dot{s}. \tag{3.7}$$

Substituting Eq. 3.3 into Eq. 3.7 yields

$$\ddot{V}_{\text{ADC}}(s, \tilde{p}) = -2s^T K_{d_{\text{ADC}}} M_p^{-1}(q_p) \left(-C_p(q_p, \dot{q}_p)s - K_{d_{\text{ADC}}} s\right) + M_p^{-1}(q_p) Y(q_p, \dot{q}_p, v, \dot{v})\tilde{p}. \tag{3.8}$$

As shown above, s and $\hat{p}$ are bounded. Boundedness of s implies that e and $\dot{e}$ are bounded. Since all reference trajectories q_p^d are bounded, v, $\dot{v}$, q_p, $\dot{q}_p$ and in turn $Y(q_p, \dot{q}_p, v, \dot{v})$ are all bounded, so it can be concluded that $\ddot{V}_{\text{ADC}}(s, \tilde{p})$ is bounded. Because all premises in Barbalat's Lemma are satisfied, $\dot{V}_{\text{ADC}}(s, \tilde{p}) \to 0$ as $t \to \infty$, which implies that the ADC guarantees asymptotic stability of the closed-loop system showing that $s \to 0$ and $q_p \to q_p^d$ for all $\tilde{p} \in \Re^r$. □

3.2 Robust Sliding Mode Adaptive Controller (RSAC)

Robustness to all parametric uncertainties, neglected dynamics, and nonzero disturbances $d_p(t)$.

Since neglected dynamics and disturbances may degrade the performance of the closed-loop system, a robust control component should be added to the ADC to compensate for these effects. The learning nature of adaptive controllers along with the existence of both disturbances and non-parametric uncertainties motivate the combination of the ADC in Section 3.1 and the RSC in [37]

to build the RSAC.

Using the same sliding surface s, signal vector v, and controller regressor $Y(q_p, \dot{q}_p, v, \dot{v})$, the control law is designed as in [36] to yield:

$$u_{p_{\text{RSAC}}} = Y(q_p, \dot{q}_p, v, \dot{v})\hat{p} - K_{d_{\text{RSAC}}} \operatorname{sat}\left(s/\operatorname{diag}(\phi)\right), \tag{3.9}$$

where ϕ represents the saturation function such that $\phi = \operatorname{diag}(\phi_1, \phi_2, ..., \phi_n), \phi_i > 0$; and $K_{d_{\text{RSAC}}}$ is a diagonal matrix with positive elements. Note that the division and saturation operations for s and $\operatorname{diag}(\phi)$ in the term $\operatorname{sat}\left(s/\operatorname{diag}(\phi)\right)$ are interpreted element-wise and $\operatorname{diag}(\phi)$ is an n-element vector. K_{d2} is a diagonal matrix with positive diagonal elements and $\hat{p}$ is estimated by a TEB adaptation law.

Substituting Eq. 3.9 into Eq. 2.10 yields

$$M_p(q_p)\dot{s} + C_p(q_p, \dot{q}_p)s + K_{d_{\text{RSAC}}} \operatorname{sat}\left(s/\operatorname{diag}(\phi)\right) = Y(q_p, \dot{q}_p, v, \dot{v})\tilde{p} + d_p(t). \tag{3.10}$$

To prevent unfavorable parameter drift in the RSAC, the following non-scalar boundary layer trajectory $s_\triangle$ is suggested [36]

$$s_\triangle = \begin{cases} 0 & \text{if } |s| \leq \operatorname{diag}(\phi) \\ s - \phi \operatorname{sat}\left(s/\operatorname{diag}(\phi)\right) & \text{if } |s| > \operatorname{diag}(\phi) \end{cases}, \tag{3.11}$$

where $s_\triangle$ is an n-element vector; and ϕ is the boundary layer thickness. The reason for incorporating $s_\triangle$ in the control structure is three-fold: (i) To stop the TEB adaptation mechanism in the boundary layer ($|s| \leq \operatorname{diag}(\phi)$), (ii) To trade off control chattering and tracking performance, and (iii) To bound all error trajectories in the boundary layers. This way, the RSAC shows robustness to parametric and non-parametric uncertainties in addition to disturbances while the error trajectories of the system converge to the boundary layer.

To prove the stability of the closed-loop system in the presence of both parametric and non-

parametric uncertainties, $Y(q_p, \dot{q}_p, v, \dot{v})$ and $\tilde{p}$ are split into two parts as

$$Y = [Y_2 \quad Y_{\text{ud}}], \qquad \tilde{p} = [\tilde{p}_2^T \quad \tilde{p}_{\text{ud}}^T], \tag{3.12}$$

where Y_2 is the modeled regressor and $\tilde{p}_2$ is its parameter vector, and Y_{ud} and $\tilde{p}_{\text{ud}}$ are associated with unmodeled dynamics of the prosthetic leg.

Consider the following Lyapunov function as a function of $s_\triangle$ and $\tilde{p}$ (as inspired from [36]):

$$V_{\text{RSAC}}(s_\triangle, \tilde{p}_2) = \frac{1}{2}\left(s_\triangle^T M_p(q_p) s_\triangle\right) + \frac{1}{2}\left(\tilde{p}_2^T \gamma \tilde{p}_2\right). \tag{3.13}$$

Theorem 2: *Assume that* $|(Y_{\text{ud}}\tilde{p}_{\text{ud}})_i| \leq P_i$, $|d_{p_i}(t)| \leq D_i$, *and* $P_i, D_i > 0$ *for* $i = 1, ..., n$. *Define* $F_m = \max(P_i + D_i)$. *Given the Lyapunov function* $V_{RSAC}(s_\triangle, \tilde{p}_2)$ *of Eq. 3.13, the RSAC control law of Eq. 3.9, and the adaptation mechanism* $\dot{\hat{p}}_2 = -\gamma^{-1} Y_2^T(q_p, \dot{q}_p, v, \dot{v}) s_\triangle$, *if control gain* $K_{d_{RSACi}} \geq F_m + \Lambda_m - \kappa \dot{q}_{p_{max}} \phi_i$ *with* $\kappa, \Lambda_m > 0$, *then* $\dot{V}_{RSAC}(s_\triangle, \tilde{p}_2) \to 0$ *as* $t \to \infty$ *for all* $p \in \Re^r$ *and* $s(0) \in \Re^n$, *which implies that* $s_\triangle \to 0$, $|s_i| \leq \phi_i$, *and* $e \leq \phi_i/\lambda_i$.

Proof of Theorem 2: Noting that $\dot{s}_\triangle = \dot{s}$ if outside the boundary layer, and substituting the error dynamics of Eq. 3.10 into the derivative of Eq. 3.13 gives

$$\begin{aligned}\dot{V}_{\text{RSAC}}(s_\triangle, \tilde{p}_2) = &- s_\triangle^T C_p(q_p, \dot{q}_p) s + \frac{1}{2}\left(s_\triangle^T \dot{M}_p(q_p) s_\triangle\right) - s_\triangle^T K_{d_{\text{RSAC}}} \operatorname{sat}\left(s/\operatorname{diag}(\phi)\right) + s_\triangle^T Y_{\text{ud}} \tilde{p}_{\text{ud}} \\ &+ \left(\dot{\tilde{p}}_2^T \gamma + s_\triangle^T Y_2\right) \tilde{p}_2 + s_\triangle^T d_p(t).\end{aligned} \tag{3.14}$$

Choosing the TEB adaptation law as $\dot{\hat{p}}_2 = -\gamma^{-1} Y_2^T s_\triangle$, substituting $s = s_\triangle + \phi \operatorname{sat}\left(s/\operatorname{diag}(\phi)\right)$ from Eq. 3.11 into Eq. 3.14 if outside the boundary layer, and applying Property 2 as

$$s_\triangle^T (\dot{M}_p(q_p) - 2C_p(q_p, \dot{q}_p)) s_\triangle = 0 \tag{3.15}$$

yields [38, 39]:

$$\dot{V}_{\text{RSAC}}(s_\triangle, \tilde{p}_2) = -s_\triangle^T(C_p(q_p, \dot{q}_p)\phi + K_{d_{\text{RSAC}}})\text{sat}\left(s/\text{diag}(\phi)\right) + s_\triangle^T\left(Y_{\text{ud}}\tilde{p}_{\text{ud}} + d_p(t)\right). \tag{3.16}$$

Tuning $K_{d_{\text{RSAC}}}$ and ϕ so $C_p(q_p, \dot{q}_p)\phi + K_{d_{\text{RSAC}}} \geq K_m I$ with $K_m > 0$, and noting that

$$s_\triangle^T\text{sat}\left(s/\text{diag}(\phi)\right) = \|s_\triangle\|_1 \tag{3.17}$$

gives

$$\dot{V}_{\text{RSAC}}(s_\triangle, \tilde{p}_2) \leq -K_m\|s_\triangle\|_1 + s_\triangle^T\left(Y_{\text{ud}}\tilde{p}_{\text{ud}} + d_p(t)\right). \tag{3.18}$$

Condition $C_p\phi + K_{d_{\text{RSAC}}} \geq K_m I$ can be restated as $K_{d_{\text{RSACi}}} \geq F_m + \Lambda_m - \kappa\dot{q}_{p_{max}}\phi_i$ (Property 3) for each joint with κ as a positive scalar and $\dot{q}_{p_{max}}$ as the maximum prosthesis joint velocity. Assume $|(Y_{\text{ud}}\tilde{p}_{\text{ud}} + d_p(t))_i| \leq P_i + D_i$ for each joint. Then, defining $F_m = \max(P_i + D_i)$, $K_m = F_m + \Lambda_m$ with $\Lambda_m > 0$, and noting that $s_\triangle^T F_m$ is upper bounded by $F_m\|s_\triangle\|_1$ yields

$$\dot{V}_{\text{RSAC}}(s_\triangle, \tilde{p}_2) \leq -\Lambda_m\|s_\triangle\|_1. \tag{3.19}$$

As Eq. 3.19 is negative semi-definite outside the boundary layer, another version of the Barbalat's Lemma is required to prove asymptotic convergence of $\dot{V}_{\text{RSAC}}(s_\triangle, \tilde{p}_2)$ to zero and in turn boundedness of the error trajectories.

Barbalat's Lemma (second version): If a function $g(t)$ is uniformly continuous[1] for all $t \geq 0$ and if the limit of the integral $\lim_{t\to\infty}\int_0^t g(h)dh$ exists and is finite, then $\lim_{t\to\infty} g(t) = 0$ [35].

Let us define

$$g(t) = \Lambda_m\|s_\triangle\|_1, \tag{3.20}$$

based on which it follows that

$$\dot{V}_{\text{RSAC}} \leq -g(t). \tag{3.21}$$

[1] A function $g(t) : \Re \to \Re$ is *uniformly continuous* on $[0, \infty]$ if $\forall\, \epsilon > 0$, $\exists\, \delta(\epsilon) > 0$, $\forall\, t_1 \geq 0$, $\forall\, t \geq 0$, $|t - t_1| < \delta \to |g(t) - g(t_1)| < \epsilon$.

Integrating both sides of Eq. 3.21 from 0 to ∞ yields

$$V_{\text{RSAC}}(0) - V_{\text{RSAC}}(\infty) \geq \lim_{t\to\infty} \int_0^t g(h)dh. \tag{3.22}$$

Since $\dot{V}_{\text{RSAC}}(t) \leq 0$, and by definition $V_{\text{RSAC}}(t) \geq 0$, the left-hand side of Eq. 3.22 is positive and finite (V_{RSAC} is bounded), which follows that the right-hand side of Eq. 3.22 exists, and is positive and finite. Hence, according to the second version of the Barbalat's lemma

$$\lim_{t\to\infty} g(t) = \lim_{t\to\infty} \Lambda_m \|s_\triangle\|_1 = 0. \tag{3.23}$$

Since $\Lambda_m > 0$, Eq. 3.23 implies that $s_\triangle \to 0$ (i.e., $|s_i| \leq \phi_i$). This implies that all error trajectories are attracted by the boundary layer if starting outside the boundary layer. On the other hand, inside the boundary layer, $s_\triangle = 0$ and s remains in the layer. □

Remark 1:

1. Note that since $s_\triangle \to 0$ and V_{RSAC} is bounded, then $\tilde{p}_2$ is bounded. Going further, since p_2 is constant, then $\hat{p}_2$ is bounded. However, it should be noted that convergence of the error trajectories to the boundary layer does not imply asymptotic convergence of $\tilde{p}_2$. Estimated parameter vector $\hat{p}_2$ asymptotically converges to its true value if $Y(q_p, \dot{q}_p, v, \dot{v})$ is persistently exciting *(PE)* and uniformly continuous [34].

2. In case that $|s| > \text{diag}(\phi)$, the adaptation law applies to the system until the unmodelled dynamics and disturbances are all compensated, resulting in the convergence of s to its ultimate bound ϕ. This implies that all error trajectories starting outside the boundary layer will converge to a small neighborhood around the origin, where the size of the neighborhood depends on the selection of the boundary layer thickness ϕ. Inside the boundary layer ($|s| \leq \text{diag}(\phi)$), $\dot{V}_{\text{RSAC}}$ can take positive sign. However when $|s| \leq \text{diag}(\phi)$, we have $s_\triangle = 0$ that inactivates the adaptation process. This ensures the boundedness p_2 and prevents the potential 'parameter drift' phenomenon. Taken altogether, the proposed controller provides

the uniformly ultimately boundedness of the system's solutions (e, p_2) regardless of starting from inside/outside the boundary layer.

3. The boundary layer thickness ϕ trades off between the tracking performance and chattering of the control signal. Although a small value of ϕ provides better tracking, it results in chattering. Adjusting the parameter λ tunes the tracking error convergence rate to achieve better tracking.

3.3 Adaptive Integral Controller (AIC)

Robustness to only parametric uncertainties, no unmodeled dynamics, and zero disturbances.

To enhance tracking performance of the ADC from Section 3.1, a different time-varying sliding surface is proposed which is the weighted sum of the position error, the velocity error, and the integral of the position error [35]:

$$s_I = \dot{e} + 2\lambda e + \lambda^2 \int_0^t e \ dt. \tag{3.24}$$

To obtain the same control law structure and error dynamics of the ADC as presented in Eqs. 3.2 and 3.3 respectively, signal vector v_I is defined as

$$v_I = \dot{q}_p^d - 2\lambda e - \lambda^2 \int_0^t e \ dt. \tag{3.25}$$

Using these error and signal vectors, the AIC control law and its error dynamics can be written as

$$u_{p_{\text{AIC}}} = Y(q_p, \dot{q}_p, v_I, \dot{v}_I)\hat{p} - K_{d_{\text{AIC}}} s_I M_p(q_p)\dot{s}_I + C_p(q_p, \dot{q}_p)s_I + K_{d_{\text{AIC}}} s_I = Y(q_p, \dot{q}_p, v_I, \dot{v}_I)\tilde{p}, \tag{3.26}$$

where $K_{d_{\text{AIC}}}$ is a diagonal matrix with positive elements.

Consider the following Lyapunov function, which is a function of s_I and $\tilde{p}$:

$$V_{\text{AIC}}(s_I, \tilde{p}) = \frac{1}{2}\left(s_I^T M_p(q_p) s_I + \tilde{p}^T \gamma \tilde{p}\right). \tag{3.27}$$

Theorem 3: *Given the Lyapunov function $V_{AIC}(s_I, \tilde{p})$ of Eq. 3.27, and the AIC control law of Eq. 3.26 in conjunction with the adaptation law $\dot{\hat{p}}_3 = -\gamma^{-1} Y^T(q_p, \dot{q}_p, v_I, \dot{v}_I) s_I$, we obtain $\dot{V}_{AIC}(s_I, \tilde{p}) \to 0$ as $t \to \infty$, which implies asymptotic stability of the closed-loop system, showing $s_I \to 0$ and $e \to 0$ for all $\tilde{p} \in \Re^r$.*

Proof of Theorem 3: Similar to the proof of Theorem 1, taking the derivative of Eq. 3.27, substituting the error dynamics of Eq. 3.26 into the result, applying the adaptation mechanism $\dot{\hat{p}}_3 = -\gamma^{-1} Y^T(q_p, \dot{q}_p, v_I, \dot{v}_I) s_I$, and using Property 2 yields

$$\dot{V}_{\text{AIC}}(s_I, \tilde{p}) = -s_I^T K_{d_{\text{AIC}}} s_I. \tag{3.28}$$

Because $\dot{V}_{\text{AIC}}(s_I, \tilde{p})$ is negative semi-definite, V_{AIC} is lower-bounded, and $\ddot{V}_{\text{AIC}}$ is bounded, using the first version of the Barbalat's Lemma as in Section 3.1 demonstrates that $\dot{V}_{\text{AIC}}(s_I, \tilde{p}) \to 0$ as $t \to \infty$. This implies that the AIC guarantees asymptotic stability of the closed-loop system, showing $s_I \to 0$ and $q_p \to q_p^d$ for all $\tilde{p} \in \Re^r$. □

Remark 2: The regressor matrix $Y(q_p, \dot{q}_p, v, \dot{v})$ is joint acceleration-independent resulting in an acceleration-free control law and adaptation mechanism for all controllers. All the proposed controllers only need joint position and velocity $(q_p, \dot{q}_p)$, and desired joint position, velocity, and acceleration $(q_p^d, \dot{q}_p^d, \ddot{q}_p^d)$. This way, there is no need to measure joint acceleration and no concern about measurement noise.

3.4 Robust Sliding Mode Controller (RSC)

Robustness to all parametric uncertainties, neglected dynamics, and existing disturbances $d_p(t)$.

The following control law is used to smooth control signal chattering, providing robustness to parameter uncertainties and unmodeled dynamics [37, 35]:

$$u_{p_{\text{RSC}}} = Y(q_p, \dot{q}_p, v, \dot{v})\hat{p} - K_{d_{\text{RSC}}} \operatorname{sat}\left(s/\operatorname{diag}(\phi)\right), \tag{3.29}$$

where $K_{d_{\text{RSC}}}$ is a diagonal matrix and $\hat{p}$ is our best knowledge of the parameter vector. The addition of $\operatorname{sat}\left(s/\operatorname{diag}(\phi)\right)$ in the above control law results in smoother control behavior in the boundary layer $|s| \leq \operatorname{diag}(\phi)$. Note that the division and saturation operations for s and $\operatorname{diag}(\phi)$ in the term $\operatorname{sat}\left(s/\operatorname{diag}(\phi)\right)$ are interpreted element-wise and $\operatorname{diag}(\phi)$ is an n-element vector.

Substituting the control law of Eq. 3.29 into Eq. 2.10 and using the definitions of s and v yields the following error dynamics:

$$\dot{s} = -M_p^{-1}\left(C_p s + K_{d_{\text{RSC}}} \operatorname{sat}(s/\operatorname{diag}(\phi)) + M_p^{-1}\left(Y(q_p, \dot{q}_p, v, \dot{v})\tilde{p} + d_p(t)\right)\right., \tag{3.30}$$

where $\tilde{p} = \hat{p} - p$ is parameter estimation error.

Using the control law of Eq. 3.29, it can be shown that all error trajectories starting outside the boundary layer will be attracted by the layer while those which start inside the boundary layer will remain inside for all $t \geq 0$ (the boundary layer is an invariant set). For this purpose, the boundary layer trajectory defined in Eq. 3.11 is employed to measure the distance between the current s to the boundary layer and also to trade off between tracking accuracy and robustness to unmodeled dynamics. The proposed control structure also satisfies the following reaching condition:

$$\frac{d}{dt} V_{\text{RSC}}(s_\triangle) \leq -\Lambda_m \|s_\triangle\|_1, \tag{3.31}$$

where $\Lambda_m > 0$.

To prove stability of the proposed controller, a scalar positive definite continuously-differentiable

Lyapunov function is considered, which is a function of $s_\triangle$

$$V_{\text{RSC}}(s_\triangle) = \frac{1}{2}\left(s_\triangle^T M_p(q_p) s_\triangle\right). \tag{3.32}$$

Theorem 4: *Assume that* $|(Y(q_p, \dot{q}_p, v, \dot{v})\tilde{p})_i| \leq Q_i$ *and* $|d_{p_i}(t)| \leq D_i$ *for* $i = 1, ..., n$ *and* $Q_i, D_i > 0$. *Define* $F_m = \max(Q_i + D_i)$. *Given the Lyapunov function* $V_{RSC}(s_\triangle)$ *of Eq. 3.32 and the RSC control law of Eq. 3.29, if* $K_{d_{RSCi}} \geq F_m + \Lambda_m - \kappa \dot{q}_{p_{max}} \phi_i$ *with* $\kappa, \Lambda_m > 0$, *then* $\dot{V}_{RSC}(s_\triangle) \to 0$ *and* $s_\triangle \to 0$ *as* $t \to \infty$ *for all* $p \in \Re^r$ *and* $s(0) \in \Re^n$, *which implies* $|s_i| \leq \phi_i$ *and the error term* $e \leq \phi_i/\lambda_i$.

Proof of Theorem 4: Taking the derivative of Eq. 3.32, noting that $\dot{s}_\triangle = \dot{s}$ if starting outside the boundary layer, and substituting the error dynamics of Eq. 3.30 into Eq. 3.32 gives

$$\dot{V}_{\text{RSC}}(s_\triangle) = -s_\triangle^T C_p s + \frac{1}{2}\left(s_\triangle^T \dot{M}_p s_\triangle\right) - s_\triangle^T K_{d_{\text{RSC}}} \operatorname{sat}\left(s/\operatorname{diag}(\phi)\right) + s_\triangle^T Y(q_p, \dot{q}_p, v, \dot{v})\tilde{p} + s_\triangle^T d_p(t). \tag{3.33}$$

Substituting $s = s_\triangle + \phi \operatorname{sat}\left(s/\operatorname{diag}(\phi)\right)$ from Eq. 3.11 into Eq. 3.33 if starting outside the boundary layer, and using the skew symmetric property $\left(s_\triangle^T(\dot{M}_p - 2C_p)s_\triangle = 0\right)$ yields [38, 39]:

$$\dot{V}_{\text{RSC}}(s_\triangle) = -s_\triangle^T(C_p\phi + K_{d_{\text{RSC}}})\operatorname{sat}\left(s/\operatorname{diag}(\phi)\right) + s_\triangle^T Y(q_p, \dot{q}_p, v, \dot{v})\tilde{p} + s_\triangle^T d_p(t). \tag{3.34}$$

Tuning $K_{d_{\text{RSC}}}$ and ϕ so $C_p\phi + K_{d_{\text{RSC}}} \geq K_m I$ (K_m is a positive scalar), and noting that

$$s_\triangle^T \operatorname{sat}\left(s/\operatorname{diag}(\phi)\right) = \|s_\triangle\|_1 \tag{3.35}$$

gives

$$\dot{V}_{\text{RSC}}(s_\triangle) \leq -K_m\|s_\triangle\|_1 + s_\triangle^T Y(q_p, \dot{q}_p, v, \dot{v})\tilde{p} + s_\triangle^T d_p(t). \tag{3.36}$$

Again condition $C_p\phi + K_{d_{\text{RSC}}} \geq K_m I$ can be restated as $K_{d_{\text{RSCi}}} \geq F_m + \Lambda_m - \kappa \dot{q}_{p_{max}} \phi_i$ (Property 3) for each joint with κ as a positive scalar and $\dot{q}_{p_{max}}$ as the maximum prosthesis joint ve-

locity. Assume $|(Y\tilde{p} + d_p(t))_i| \leq P_i + D_i$ for each joint. Then, defining $F_m = \max(P_i + D_i)$, $K_m = F_m + \Lambda_m$ with $\Lambda_m > 0$, and noting that $s_\triangle^T F_m$ is upper bounded by $F_m \|s_\triangle\|_1$ yields

$$\dot{V}_{\text{RSC}}(s_\triangle) \leq -\Lambda_m \|s_\triangle\|_1. \tag{3.37}$$

Therefore, if error trajectories start outside the boundary layer, $\dot{V}_{\text{RSC}}(s_\triangle) \to 0 \Rightarrow s_\triangle \to 0$. In turn, the distance between s and the boundary layer approaches zero, showing that s is attracted by the boundary layer. This result implies that $|s_i| \leq \phi_i$ and $e \leq \phi_i/\lambda_i$ proving stability of the prosthesis / RSC combination and boundedness of the tracking error trajectories by the boundary layer (regardless of starting point). □

3.5 Robust Passivity Controller (RPC)

Robustness to only parametric uncertainties and unmodeled dynamics (assuming $d_p(t) = 0$).

With the definitions of error and signal vectors, and the acceleration-free controller regressor in hand, the RPC is presented based on passivity in parameters and a switching control law [27]:

$$u_{p_{\text{RPC}}} = Y(q_p, \dot{q}_p, v, \dot{v})\hat{p} - K_{d_{\text{RPC}}} s, \tag{3.38}$$

where $K_{d_{\text{RPC}}}$ is a diagonal matrix with positive diagonal entries.

Substituting Eq. 3.38 into Eq. 2.10, and defining $\hat{p} = p_0 + u_b$ and $\tilde{p} = p_0 - p$ yields the error dynamics

$$\dot{s} = -M_p^{-1}\left(C_p s + K_{d_{\text{RPC}}} s\right) + M_p^{-1} Y(q_p, \dot{q}_p, v, \dot{v})(\tilde{p} + u_b), \tag{3.39}$$

where p_0 is the nominal parameter vector, $\|\tilde{p}\| \leq \rho$, $\rho \geq 0$, and auxiliary control term u_b can be defined as [27]

$$u_b = \begin{cases} -\rho r/\|r\| & \text{, if } \|r\| > \epsilon \\ -\rho r/\epsilon & \text{, if } \|r\| \leq \epsilon \end{cases}, \tag{3.40}$$

where $r = Y^T(q_p, \dot{q}_p, v, \dot{v})s$.

Consider the following scalar positive definite Lyapunov function:

$$V_{\text{RPC}}(s, e) = \frac{1}{2}\left(s^T M_p(q_p)s + e^T \lambda K_{d_{\text{RPC}}} e\right). \tag{3.41}$$

Theorem 5: *Let* $Q = \text{diag}(\lambda^T K_{d_{RPC}}\lambda, K_{d_{RPC}})$. *Given the Lyapunov function* $V_{RPC}(s, e)$ *of Eq. 3.41, the RP controller of Eq. 3.38, and the auxiliary control term* u_b *of Eq. 3.40, if* $\|r\| > \epsilon$, *or* $\|r\| \leq \epsilon$ *and the error term has the property that* $\|e\| \geq \sqrt{\rho\epsilon/2\lambda_{\min}(Q)}$, *then* $\dot{V}_{RPC}(s, e) \to 0$ *as* $t \to \infty$ *for all* $\tilde{p} \in \Re^r$, *which implies boundedness of all tracking error trajectories.*

Proof of Theorem 5: Taking the derivative of Eq. 3.41, substituting the error dynamics of Eq. 3.39, and using the skew symmetric property $\left(s^T(\dot{M}_p - 2C_p)s = 0\right)$ gives

$$\dot{V}_{\text{RPC}}(s, e) = s^T Y(q_p, \dot{q}_p, v, \dot{v})(\tilde{p} + u_b) - e^T \lambda^T K_{d_{\text{RPC}}} \lambda e - \dot{e}^T K_{d_{\text{RPC}}} \dot{e}. \tag{3.42}$$

Using the definition of r yields

$$\dot{V}_{\text{RPC}}(s, e) = r^T(\tilde{p} + u_b) - e^T Q e. \tag{3.43}$$

If $\|r\| > \epsilon, \quad u_b = -\rho r/\|r\|$

$$\dot{V}_{\text{RPC}}(s, e) \leq \|r\|\tilde{p} - \rho\|r\| - e^T Q e \tag{3.44}$$

and it can be concluded that $\dot{V}_{\text{RPC}}(s, e) < 0$ using the Cauchy-Schwartz inequality $(\|r\|(\tilde{p}-p) \leq 0)$.

On the other hand, if $\|r\| \leq \epsilon$, then $u_b = -\rho r/\epsilon$ and

$$\dot{V}_{\text{RPC}}(s, e) \leq \|r\|\tilde{p} - \rho\|r\|^2/\epsilon - e^T Q e. \tag{3.45}$$

Table 3.1: Characteristics of the proposed controllers

Controller	Adaptation to system parameters	Robustness to unmodeled dynamics	Robustness to disturbances
ADC	✓	×	×
RSAC	✓	✓	✓
AIC	✓	×	×
RSC	×	✓	✓
RPC	×	✓	×

Noting that $\|r\|\tilde{p} - \rho\|r\|^2/\epsilon$ is upper bounded by $\rho\epsilon/2$, $\dot{V}_{\text{RPC}}(s, e) < 0$ if

$$e^T Q e > \rho\epsilon/2. \tag{3.46}$$

As $e^T Q e$ is upper bounded by $\lambda_{\max}(Q)\|e\|^2$ and lower bounded by $\lambda_{\min}(Q)\|e\|^2$, the condition of Eq. 3.46 can be rewritten as

$$\|e\| \geq \sqrt{\frac{\rho\epsilon}{2\lambda_{\min}(Q)}}. \tag{3.47}$$

Therefore, using the control law of Eq. 3.38, the term $r^T(\tilde{p} + u_b)$ in Eq. 3.43 is forced to be non-negative, regardless of the lack of information about $\tilde{p}$, which results in $\dot{V}_{\text{RPC}}(s, e) < 0$. That is, the prosthesis / RPC emulates humanlike walking with the bounded tracking error trajectories. □

Table 3.1 summarizes the characteristics of all five proposed controllers that whether or not they are able to compensate/estimate the parametric uncertainties, unmodeled dynamics, and external disturbances.

CHAPTER 4

SIMULATION RESULTS ON VIRTUAL HUMAN/ROBOT SYSTEM

In this section, we evaluate all five proposed controllers for the walking biped platform shown in Fig. 1.2, while both body and prosthesis device parameters are unknown to the controllers. As mentioned above, the proposed controllers are only used to control the prosthetic knee while the rest of the joints are controlled by the feedback linearization human-inspired controller [26]. This coincides with the fact that in practice, all joints can be controlled by the human except amputated joints. Recall that in Section 2, the desired prosthesis trajectory, q_p^d, was derived via optimization and the PHZD reconstruction procedure. All the proposed controllers are then compared to each other with regard to tracking performance and robustness to unexpected push and obstacle disturbances.

Remark 3: The design parameters of all model-based controllers are listed in Table 4.1. We tune the design parameters of each controller to achieve the best trade-off between tracking accuracy and robustness to disturbances $d_p(t)$ and neglected dynamics. Specifically, tuning the parameters for each controller is based on the following concepts: increasing λ improves tracking; increasing K_d enhances stability and robustness; decreasing γ improves adaptation convergence rate; and ϕ and ϵ make a trade off between tracking and chattering.

4.1 Tracking Performance and Humanlike Walking

Figures 4.1 illustrates prosthetic knee tracking performance for all proposed controllers over two steps. However, note that the entire simulation runs for 40 steps. It can be observed that all controllers track the desired trajectories in both stance and non-stance phase. Figure 4.2 provides phase portraits for the stance and non-stance knee joints over 40 steps. The phase portraits show convergence of the controllers to a stable limit periodic orbit. It can also be seen from a careful inspection that the most consistent portraits belong to the ADC and AIC, showing the best tracking

Table 4.1: Design parameters of the model-based controllers in the simulation and experiments: (simulation, experiment). These parameters are tuned to achieve the best trade-off between tracking performance and robustness as described in Remarks 3 and 5.

Controller	Parameter	Stance	Non-stance
ADC	λ	(40I, 40I)	(40I, 35I)
	K_{d1}	(40I, 50I)	(40I, 35I)
	γ	(0.01I, 0.01I)	(1000I, 1000I)
RSAC	λ	(40I, 50I)	(40I, 50I)
	K_{d2}	(100I, 100I)	(100I, 100I)
	γ	(0.1I, 0.1I)	(1000I, 1000I)
	ϕ	(2I, 4I)	(2I, 4I)
AIC	λ	(30I, 25I)	(30I, 35I)
	K_{d3}	(40I, 40I)	(40I, 40I)
	γ	(0.1I, 0.01I)	(1000I, 1000I)
RSC	λ	(50I, 40I)	(30I, 30I)
	K_{d4}	(50I, 40I)	(30I, 30I)
	ϕ	(0.5I, 1I)	(0.5I, 1I)
RPC	λ	(30I, 25I)	(10I, 10I)
	K_{d5}	(40I, 35I)	(20I, 20I)
	ϵ	(10000, 10000)	(10000, 10000)

performance with more appropriate velocity at impact compared to other controllers. The impact upon foot strike induces a larger knee velocity change with the RSC and RPC (roughly 0.6 rad/s velocity jump when the stance knee angle is 0.35 rad) than the others. Furthermore, when impact occurs, the RSAC produces a higher negative knee velocity (approximately 1 rad/s higher velocity than the others at the end of swing phase), resulting in a highly variable phase portrait.

4.2 Robustness Tests

To test the stability of the virtual human/prosthesis system and quantify human/prosthesis system robustness in the presence of disturbances (unexpected pushes and obstacles as shown in Fig. 4.3), two robustness tests are performed for all proposed controllers and the results are compared with each other. For the first robustness test, pushes are applied to the prosthetic leg in both x-direction and z-direction (with respect to the combined system world frame $O_{co} = \{x_{co}, y_{co}, z_{co}\}$ shown in Fig. 4.3).

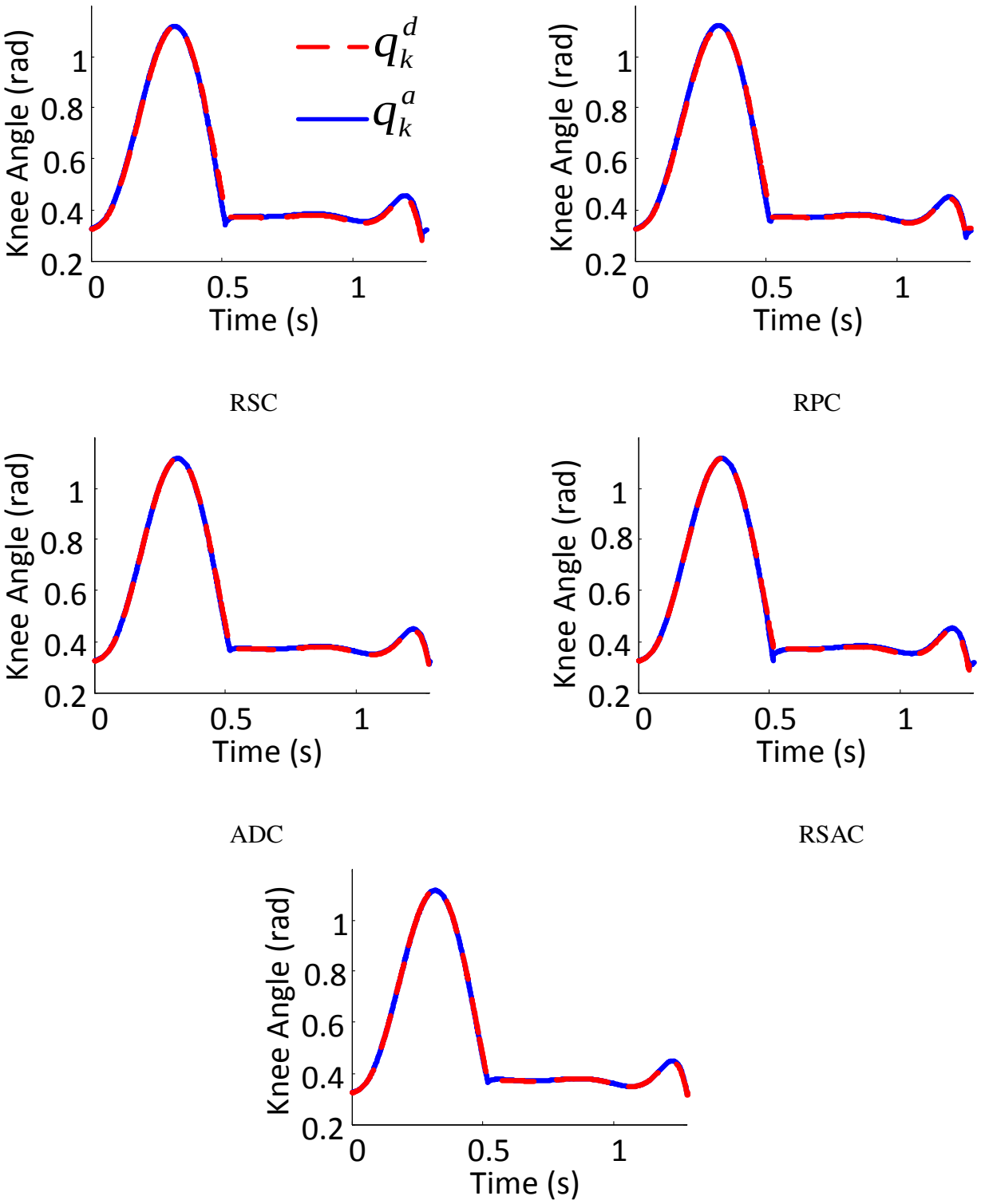

Figure 4.1: Tracking performance of the prosthetic knee joint over two steps for different model-based controllers

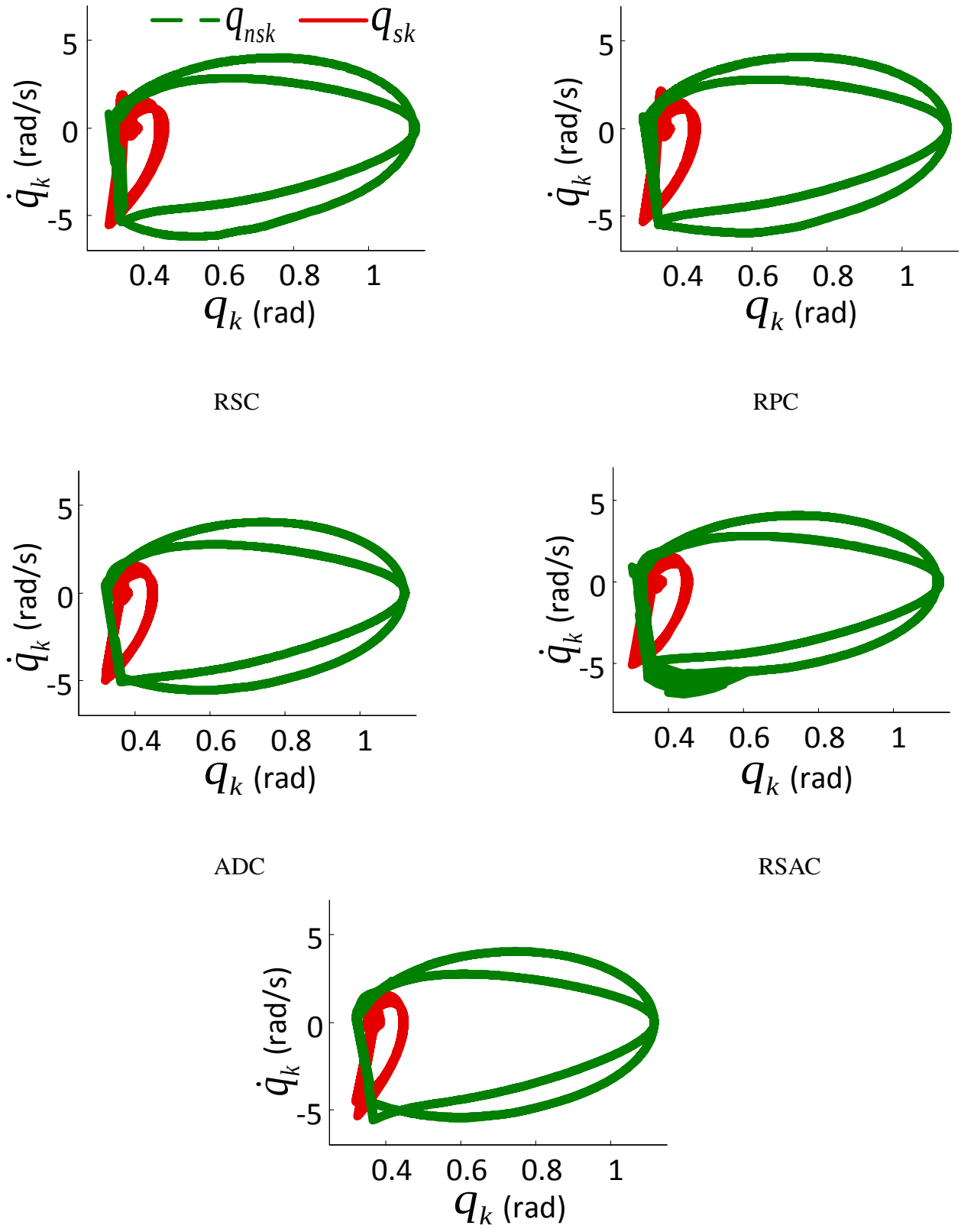

RSC RPC

ADC RSAC

AIC

Figure 4.2: Phase portraits of the prosthetic knee joint over 40 steps for different model-based controllers

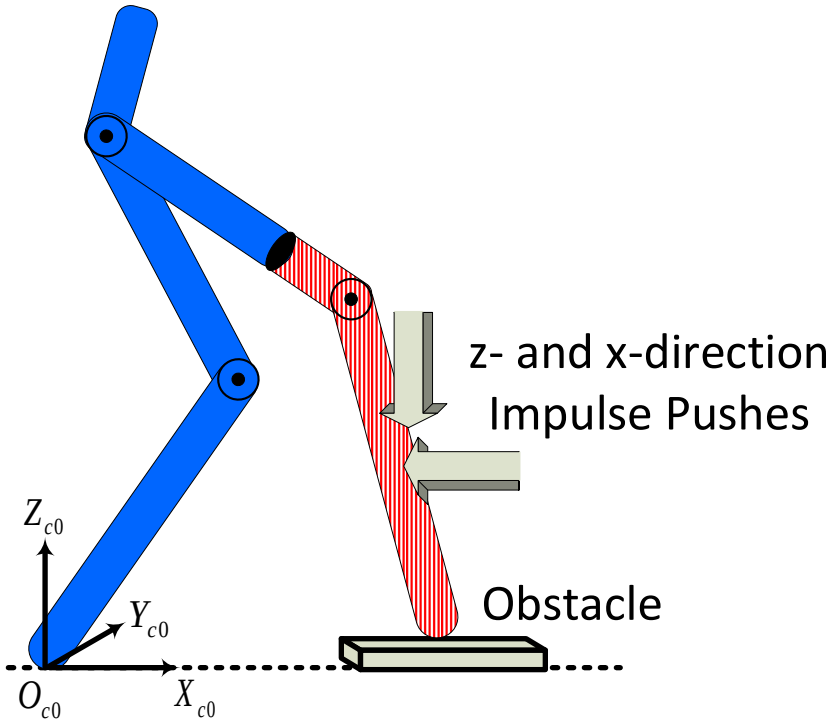

Figure 4.3: Robustness test with push and obstacle disturbances

4.2.1 Robustness to Impulse Force

For the first test, an x-direction impulse (lasting for 0.01 sec) is applied to the prosthetic leg for 40 steps each time it begins to swing forward. Figure 4.4 depicts the phase portrait of the system under all control approaches during the test. Beginning with the RSC, the maximum tolerated force is determined to be 60 N. It can be observed that the non-stance knee phase portrait deviates when the x-direction force is applied, but then smoothly converges to the cycle. This implies that the RSC can consistently tolerate the applied x-direction disturbance.

A similar test is also performed for the other controllers, but these controllers are not able to tolerate the same 60 N force in the x-direction, causing the system to fall at some point during the walking. The force of the impulse is then iteratively decreased with a resolution of 1 N until it can be tolerated. Figure 4.4 shows convergence of all other controllers' phase portraits after reducing the force during each prosthetic swing for each individual controller.

Similarly, a 30 N z-direction force is applied during prosthetic swing for all controllers for 40

steps. The RSC shows a good robustness to this force by completing 40 steps, while simulation with other controllers fails again. Figure 4.5 demonstrates convergence of all controllers to the cycle when the z-direction force applied to the other controllers is reduced. Figures 4.4 and 4.5 also show a sharper velocity change on the phase portraits of the RPC, ADC, and AIC compared to the RSC and RSAC when z- and x-direction forces are applied to the prosthetic leg.

4.2.2 Robustness to Obstacles

For the second robustness test, the human/prosthesis system is forced to walk over an obstacle for 40 steps. Figure 4.6 demonstrates two steps of the actual and desired prosthesis knee angles captured during walking for all controllers at the point when the obstacle appears. For each controller, an unexpected obstacle appears each step during the prosthesis stance phase (see video available at [24]). From this figure, it is seen that the RSC and RSAC can overcome the 20 mm obstacle, while other controllers can not walk over the same 20 mm obstacle. The height of the obstacle is iteratively decreased with a resolution of 1 mm until it can be walked over. It should be noted that when the biped walks over the obstacle, its next swing step tends toward greater knee extension no matter which controller is used.

To better characterize the controller responses, Fig. 4.6 shows arrows demonstrating the exact moment the obstacle is encountered. From this figure, it is easily observed that ADC and RPC quickly converge to the desired trajectory after encountering the obstacle, RSC and RSAC have a more sluggish response, and the AIC has the worst convergence.

4.2.3 Numerical Discussion

Table 4.2 lists root mean square error (RMSE) values for prosthetic knee tracking using all controllers and corresponding maximum disturbance tolerated (MDT) in the robustness tests for 40 steps.

This table shows that the RSC provides the poorest knee tracking and the AIC provides the best. The AIC achieves 70% better tracking than the RSC. As tracking and robustness performances

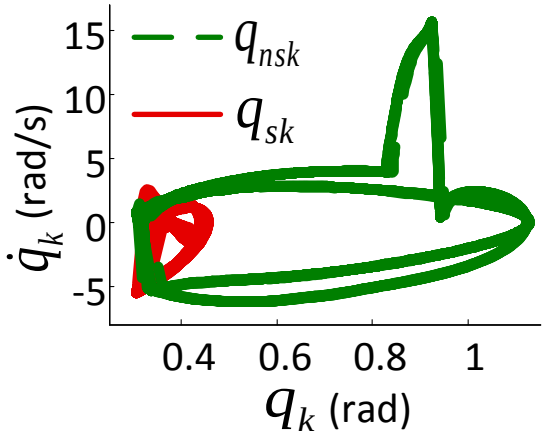

RSC with F_x=60 N

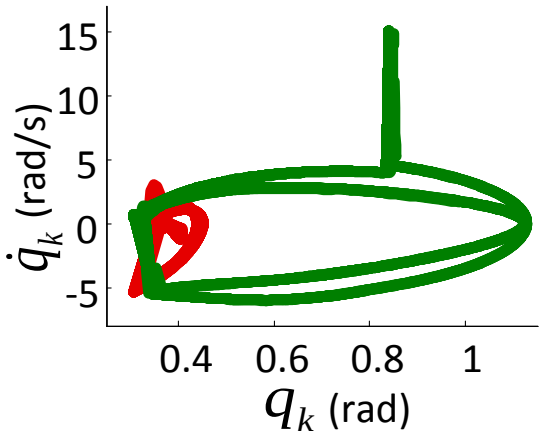

RPC with F_x=25 N

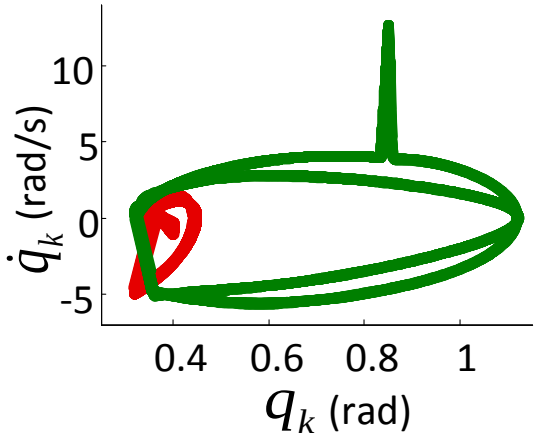

ADC with F_x=15 N

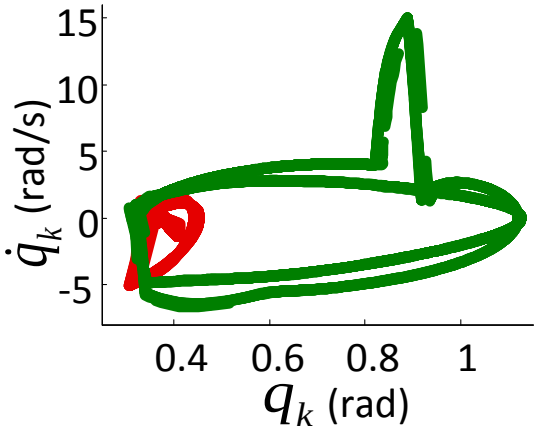

RSAC with F_x=35 N

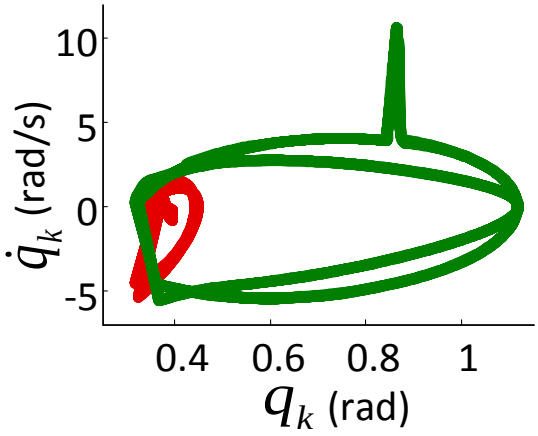

AIC with F_x=10 N

Figure 4.4: Phase portrait of the knee joint over 40 steps with the applied impulse force in the x-direction F_x at different levels using different model-based controllers

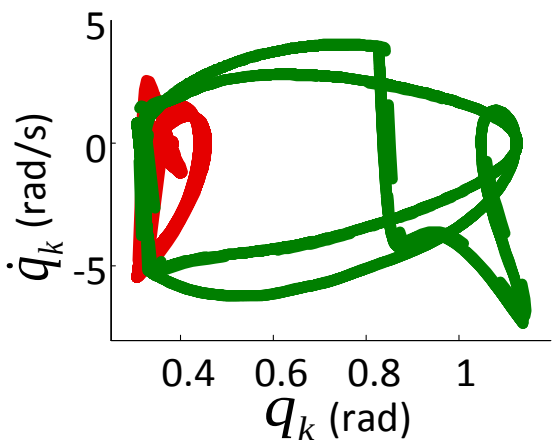

RSC with F_z=30 N

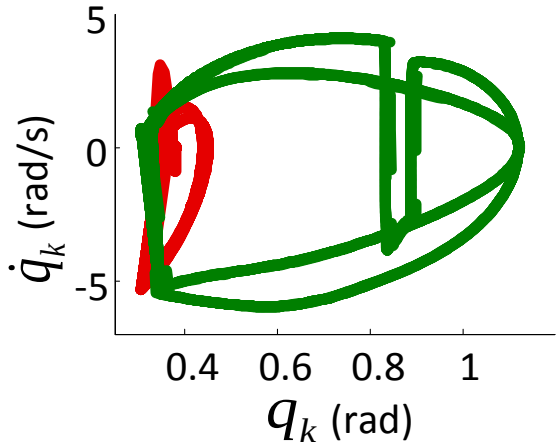

RPC with F_z=5 N

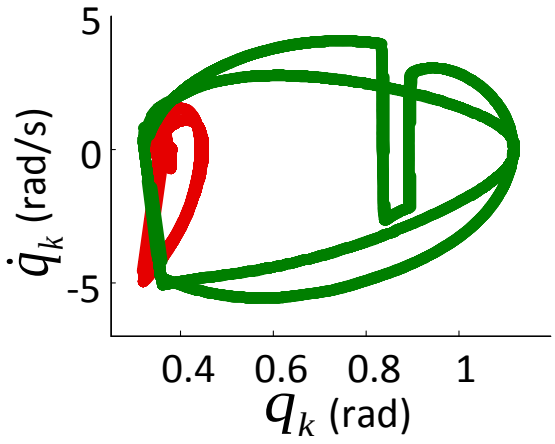

ADC with F_z=3 N

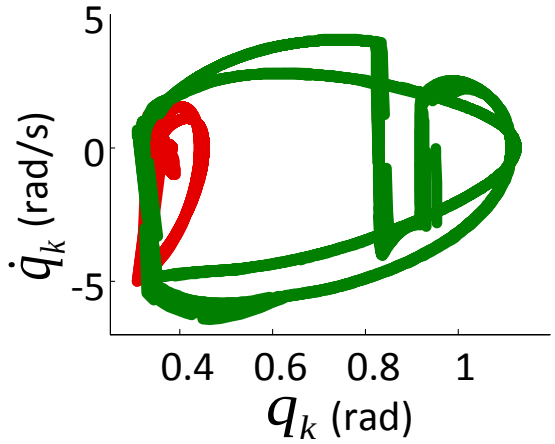

RSAC with F_z=8 N

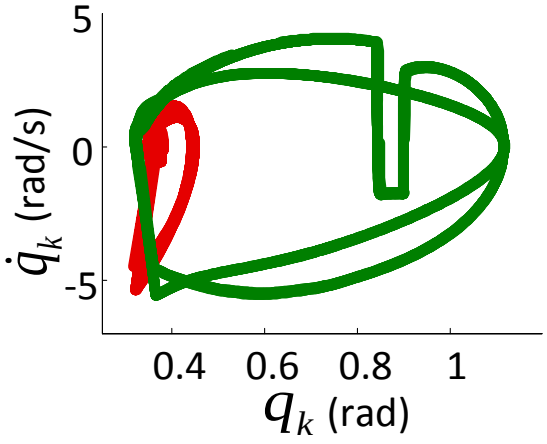

AIC with F_z=2 N

Figure 4.5: Phase portrait of the knee joint over 40 steps with the applied impulse force in the z-direction F_z at different levels using different model-based controllers

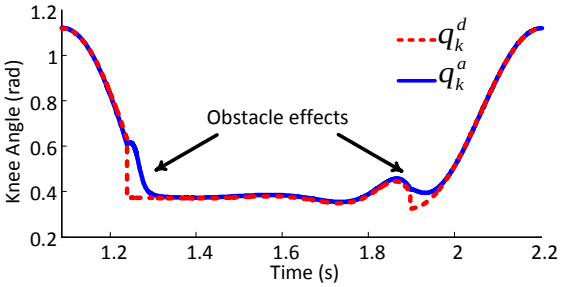

RSC, 20 mm

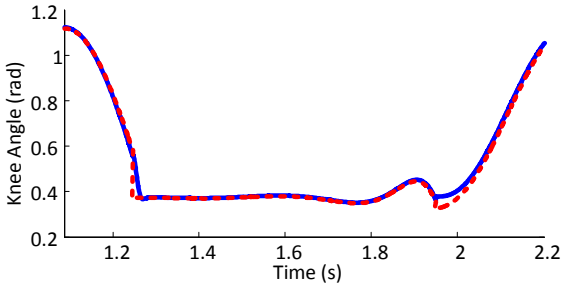

RPC, 15 mm

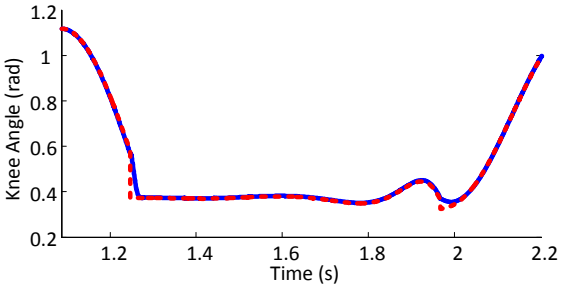

ADC, 15 mm

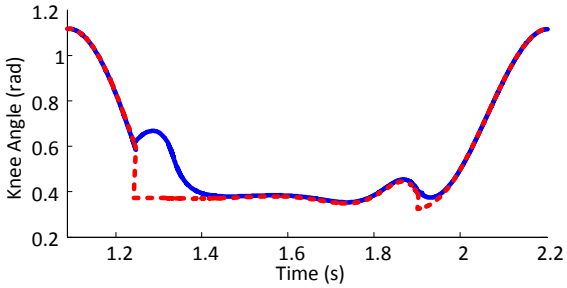

RSAC, 20 mm

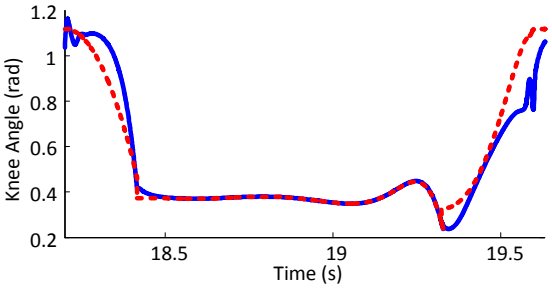

AIC, 5 mm

Figure 4.6: Prosthetic knee angle using different model-based controllers when the system walks over the obstacle. Note that different controllers overcome the obstacles with different heights in mm.

Table 4.2: Tracking results and robustness performance for the proposed controllers. The best value for each metric is underlined.

	RSC	RPC	ADC	RSAC	AIC
$\mathrm{RMSE}_{\mathrm{40Steps}}$ (rad)	0.0124	0.0111	0.0043	0.0059	<u>0.0037</u>
$\mathrm{MDT}_{\mathrm{Force_x}}$ (N)	<u>60</u>	25	15	35	10
$\mathrm{MDT}_{\mathrm{Force_z}}$ (N)	<u>30</u>	5	3	8	2
$\mathrm{MDT}_{\mathrm{Obstacle}}$ (mm)	<u>20</u>	15	15	<u>20</u>	5

are conflicting objectives, the RSC outperforms the other controllers with regard to robustness to pushes and obstacle disturbances, whereas the AIC ranks last in robustness.

According to Table 4.2, the RSAC has the same level of robustness to obstacles as the RSC while performing second best in terms of robustness to pushes. The greater robustness of the RSC and RSAC in simulation is supported by the proofs in Section 3. Recall that stability of RSC and RSAC is mathematically proven in the presence of time-varying disturbance $d_p(t)$, whereas stability of other proposed controllers can not be guaranteed in the presence of external disturbances.

As also seen from the proofs in Section 3, the AIC and ADC can only deal with parametric uncertainties and the RPC can only handle parametric uncertainties and unmodeled dynamics but not exogenous disturbances. However, the ADC, AIC, and RPC are still able to show some robustness to the disturbances. It should be noted that the AIC has the worst robustness to disturbances, whereas the best tracking of this controller comes from its integral operation.

According to Table 4.2, the RSAC is able to achieve the best trade-off between tracking and robustness, in line with its main goal of achieving acceptable tracking performance while providing good robustness to all parametric uncertainties, unmodeled dynamics, and disturbances. As seen from the tracking results and robustness tests, the RSC provides the best robustness and stability in the presence of disturbances, the AIC provides the best tracking performance, and the RSAC provides the best compromise between these goals.

CHAPTER 5
EXPERIMENTAL RESULTS ON AMPRO3

In this section, all proposed controllers are tested experimentally using the powered self-contained transfemoral prosthesis AMPRO3 on a treadmill, as shown in Fig. 5.1, and compared two popular model-free controllers: VI and PD. Finally, outdoor tests are carried out to demonstrate walking in the real world.

5.1 Detailed Description of AMPRO3 Mechanical Design

This device has two 206 W brushless DC motors (MOOG BN23) to actuate ankle and knee flexion/extension joints. A pair of torsion springs is incorporated between the harmonic gearbox and joints, resulting in series elastic actuators (SEA). The reason for using the torsion springs is threefold: (i) To increase comfort for the user, (ii) To prevent impacts from transferring directly to the gearboxes/motors, preventing damage, and (iii) To improve energy efficiency and make walking speed acceleration easier.

In AMPRO3, motor and gearbox are separated from each other with a pulley-belt driven transmission system. The reason for this design is two-fold: (i) A greater gear reduction ratio can be achieved by choosing differently sized pulleys, resulting in a smaller and lighter harmonic gearbox, and (ii) A pulley-belt transmission isolates the motors from direct impact shocks. AMPRO3 uses two ELMO motion controllers (Gold Solo Whistle) to drive the motors with low-level torque control. Two encoders are used at both knee and ankle joints and connected to ELMO drives for motor control and joint feedback information.

A passive ankle roll joint is used for lateral ankle movement for comfort and for more natural 3D gait. AMPRO3 uses a 9-cell Lipo battery (ThunderPower) to power the device. A 6-axis load cell is incorporated in series between the calf and the foot. Two flex force sensors are used for on and off ground contact conditions. The total weight of AMPRO3 is 5.95 Kg (without knee adapter)

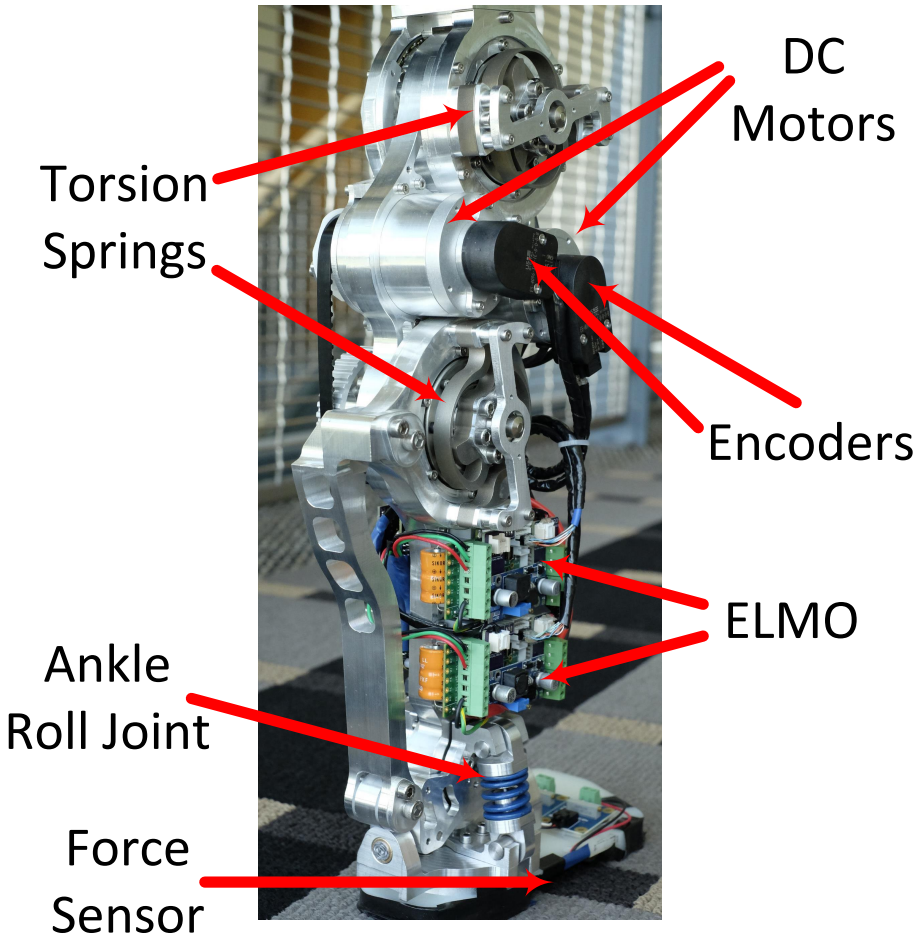

Figure 5.1: AMPRO3 device with its components

and the total height is 451 mm. AMPRO3 and its components are shown in Fig. 5.1 and further details about the device can be found in [31, 40].

5.2 Control Architecture

The control architecture of the AMPRO3 device comprises three levels. (i) low-level control is handled by the ELMO motion drives to compensate for unmodeled dynamics such as friction, damping effects, and transmission dynamics of the motors; (ii) mid-level control computes the input torques for the joints; and (iii) high-level control is responsible for robot/human interaction. We code high-level controllers and trajectories in C++ using Robot Operating System (ROS) packages. Trajectories and controller outputs are calculated by a single Beaglebone Black (BBB) at 200

Hz.

ROS includes many helpful modules for robotic control and data visualization (e.g., rviz). While ROS is widely used throughout multi-agent robotic swarms and humanoid robots, in this work, it is primarily used only for control loop parallelization and setting initial startup conditions. Upon startup, the ROS Master node populates the parameter server with initial conditions, facilitating quick debugging and allowing testing without a recompilation. There exist separate nodes for collecting sensor data, one each for the encoders and force sensors. The entire ROS implementation, including simple message passing between the sole control node and master node, operates natively on the BeagleBone single board computer. The most important portions of the control code are expressed as controller definitions in this work, and other implementation details are derived from hardware libraries provided by the manufacturers.

5.3 Test Procedure

The functional reach test (FRT) and two minute walk (2MW) test are two widely accepted tests for quantifying the performance of prostheses. The FRT is usually used to test for balance [41]. However, the primary investigation of this work is not static posture stability, but rather prosthetic knee dynamics during walking. The 2MW test is a test of endurance which evaluates metabolic capacity [42]. Importantly, the main independent variable is often distance covered when walking. The intent of this study is not to characterize the role of fatigue during walking, but rather to isolate the behaviors of the prosthesis controllers and their relationship to simulated values. Again, we elect not to perform the 2MW test because the objective is not to quantify the effects of fatigue on distance traveled. Instead, we choose to allow the subjects to walk for 2.5 minutes at a leisurely pace to allow them time to acclimate to the device. In this study, the treadmill is speed-controlled for the purpose of test consistency. The representative periods of prosthesis data used in the comparisons are chosen for their consistency from step-to-step, as human model inputs in the simulation are also constant.

We test the proposed controllers using an able-bodied subject on a treadmill and compare them

with VI and PD controllers. It should be pointed out that in experiments, the prosthetic knee joint is controlled by the proposed controllers while the ankle joint is controlled by a PD controller to act like a passive joint, emulating the point foot conditions used during simulation [37]. For this purpose, a simple PD controller with small coefficients for the ankle is employed with the goal of modeling the prosthetic ankle as a passive spring-damper mechanism (i.e., small rotation of the ankle).

During the treadmill experiments, an able-bodied subject wears the prosthesis with a bent-knee adapter as shown in Fig. 1.1 and walks on the treadmill for 2.5 min at 2 mph. For ease of implementation and reduction of noise, the hip horizontal and vertical positions (q_{p1} and q_{p2} respectively), and thigh angle (q_{p3}) of the prosthetic device modeled in Section 2.2 are considered to be their desired values in the controller rather than values from IMU measurements. Finally, three test subjects are asked to walk with AMPRO3 on level ground, uphill slopes, and downhill slopes in different outdoor environments as will be discussed at the end of this section.

5.4 Implementation of the VI and PD Controllers

5.4.1 Variable Impedance Controller (VI)

Because the VI controller is model-free, the prosthetic knee torque during a single stride (one gait cycle) can be generated using only local information of the knee joint modeled as series of passive impedance functions. In this approach, one stride is divided into several sub-phases, and each sub-phase is controlled by its own impedance controller. In this work, one gait cycle is separated into three phases denoted $p \in \{1, 2, 3\}$, i.e., one for stance (p^1), one for swing back (p^2), and one for swing forward (p^3).

The prosthetic knee torque of the VI controller is generated from

$$u_{VI}^{p} = k^{p}(q_{knee} - q_{e}^{p}) + b^{p}\dot{q}_{knee}, \tag{5.1}$$

where q_{knee} and $\dot{q}_{knee}$ are angle and angular velocity of the prosthetic knee joint; p is phase

number; and k^p, q_e^p, and b^p are phase-specific stiffness, damping, and equilibrium angle values respectively. Therefore, a total of nine parameters must be tuned for the VI controller as $k^p = (-250.81, -15.91, -25.31)$, $b^p = (-21, 1.68, 2.82)$, and $q_e^p = (0.40, 1, 0.28)$ for (p^1, p^2, p^3). Tuning parameters of the VI controller is a challenging task that requires an expert to achieve good performance.

5.4.2 Proportional-Derivative Controller (PD)

In the experiments, the prosthetic knee torque of the PD controller is generated from

$$u_{PD} = -k_p e_{knee} + k_d \dot{e}_{knee}, \tag{5.2}$$

where k_p and k_d are design parameters. Since the effect of gravity is unknown to the PD controller, the control law of Eq. 5.2 yields steady state error on the prosthetic knee joint tracking. The tuning process of the PD controller is fairly straightforward. Increasing k_p decreases the steady state error but may degrade the stability and increase overshoot. k_d also affects the stability of the system and improves it if the value is small. The design parameters of the PD controller in both stance and non-stance phases are tuned as $k_p = 100$ and $k_d = 20$.

Remark 4: The design parameters of all proposed controllers in the experiments are listed in Table 4.1. In the experiments, we initially use the same parameter values from simulation. We then tune the parameters within a small variation to achieve comfortable and sustainable walking. Table 4.1 confirms that the design parameters from the simulation can be directly applied to the prosthesis with minimal parameter tuning. The discrepancy between the parameter values in simulation and experiments stems from the hardware limitations and unmodeled dynamics between the model of Fig. 1.2 and the real human/prosthesis system. Thus, to achieve the best performance during experiment, design parameters need to be tuned with a small change from the simulation values.

5.5 Experimental Results

5.5.1 Treadmill Test

Figures 5.2 and 5.3 demonstrate tracking performance of all model-based controllers over 2.5 minutes of walking for two consecutive steps along with their corresponding phase portraits. From Fig. 5.2, it can be seen that all proposed controllers are able to track the prosthetic knee joint trajectories. Figure 5.3 shows that the system with the model-based controllers provides stable limit cycles. However, the AIC and ADC yield better knee angle tracking, while the RSC and RSAC provide the cleanest phase portraits, demonstrating greater consistency and robustness. Figure 5.4 demonstrates tracking results and phase portraits of the prosthetic knee joint using the VI and PD controllers for 2.5 min of walking. This figure shows that all proposed model-based controllers outperform both VI and PD controllers in tracking. Compared to the VI controller, the PD controller performs better regarding tracking performance and stability of the limit cycle.

Figure 5.5 compares prosthetic knee torques for the proposed controllers VI and PD controllers for a randomly selected time period $t \in [28, 30]$ sec. It can be seen that all the controllers generate similar absolute peak torque values at the end of the swing phase while a numerical comparison in Table 5.1 shows that the RSAC uses the lowest maximum torque value. Figure 5.6 shows gait tiles of the human-prosthesis system walking in simulation and also experimentally using AMPRO3 with an able-bodied human test subject for all model-based controllers, visually demonstrating humanlike walking.

5.5.2 Numerical Results for Treadmill Test

Table 5.1 lists RMSE, maximum tracking error E_{max}, maximum torque value τ_{max}, the RMS of the knee torque RMS_τ, number of the design parameters $\mathrm{N_p}$, and tuning time of these parameters $\mathrm{t_t}$ for AMPRO3 walking using the proposed controllers. This table also compares the results with VI and PD controllers over 2.5 min of walking. The best value for each metric is underlined in the table, showing that the best tracking performance and lowest E_{max} are achieved by the AIC, the

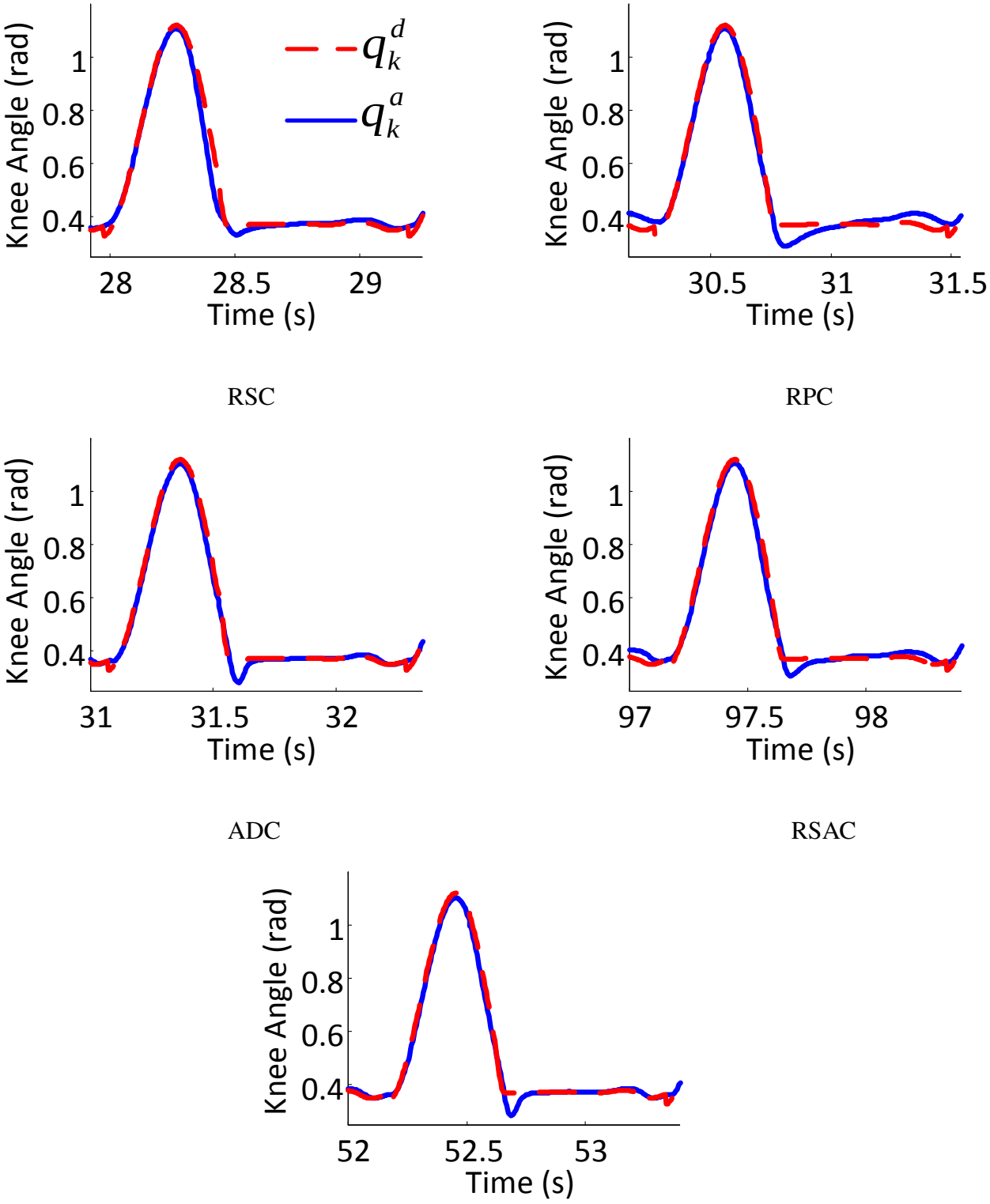

Figure 5.2: Experimental tracking performance of the prosthetic knee joint for 2.5 min of walking on a treadmill using different proposed controllers

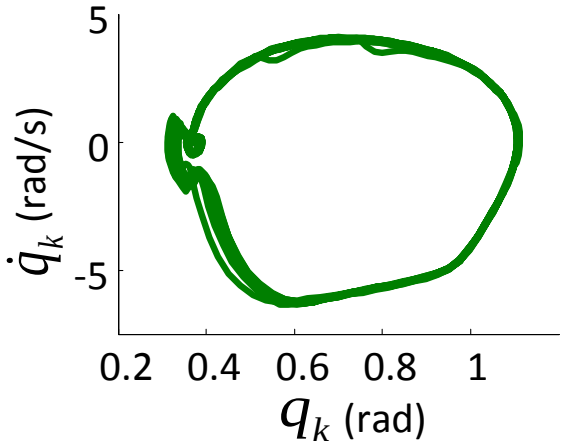

RSC

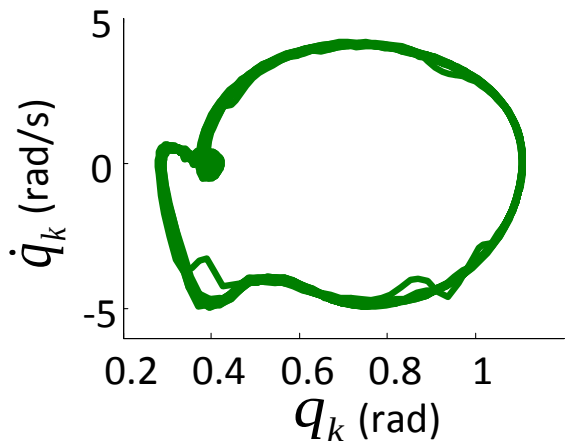

RPC

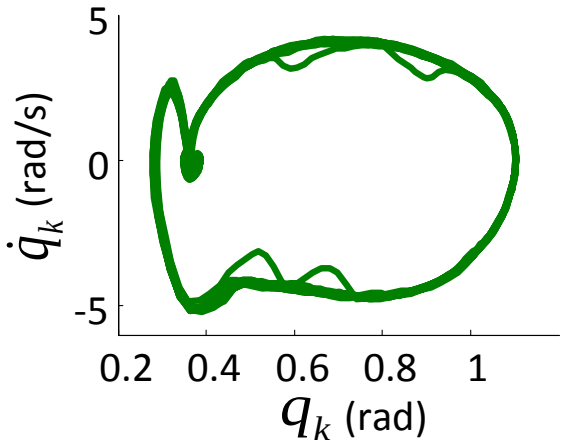

ADC

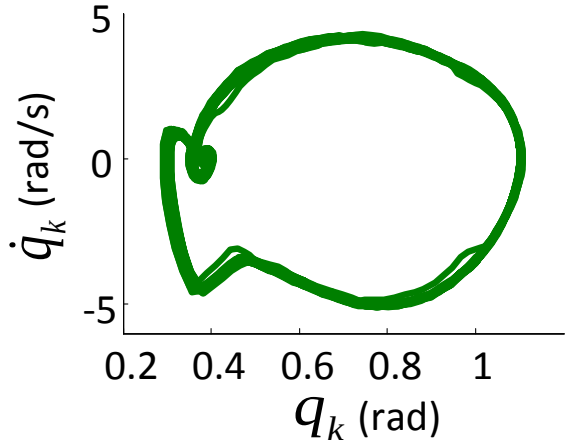

RSAC

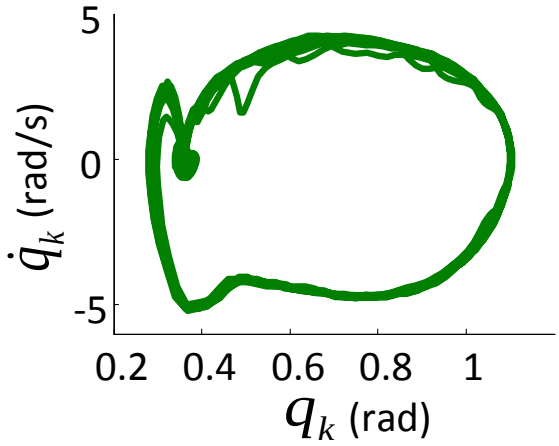

AIC

Figure 5.3: Experimental phase portrait of the prosthetic knee joint for 2.5 min of walking on a treadmill using different proposed controllers

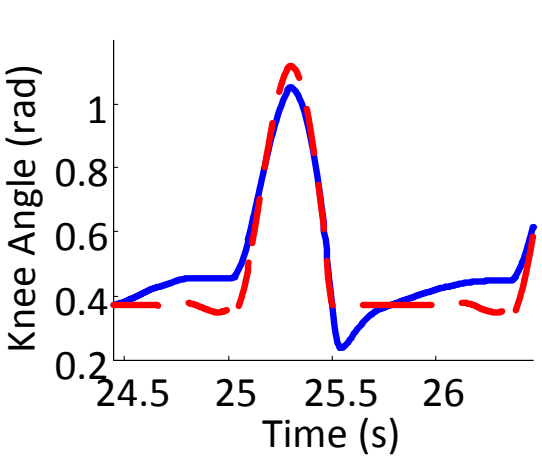

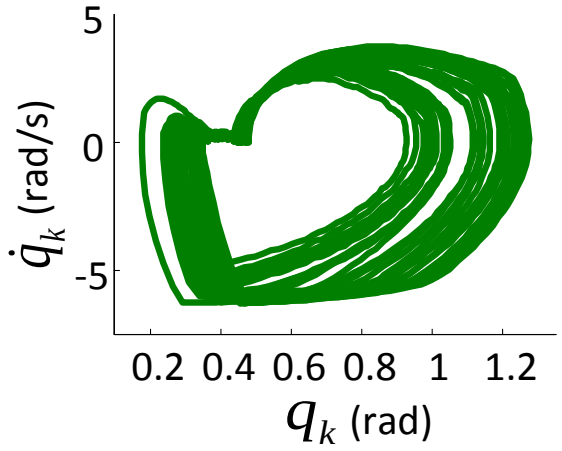

VI

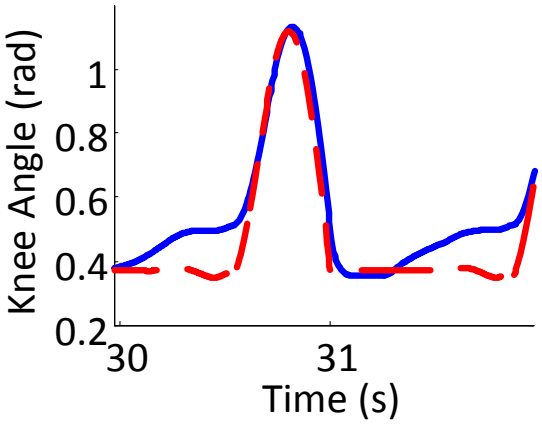

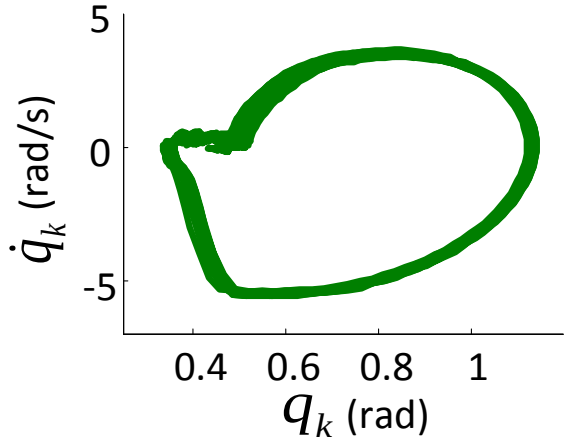

PD

Figure 5.4: Experimental tracking performance and phase portrait of the prosthetic knee joint for 2.5 min of walking on a treadmill using VI and PD controllers

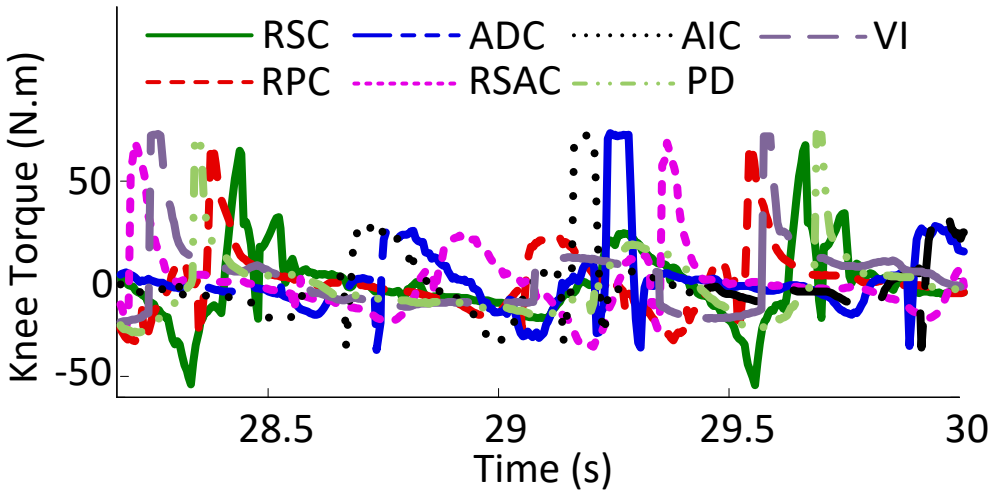

Figure 5.5: Experimental prosthetic knee torque comparison between all proposed approaches, and VI and PD controllers for a treadmill test

Table 5.1: Experimental results of AMPRO3 using the five proposed approaches as well as VI and PD controllers over 2.5 min of walking on a treadmill. The best value for each metric is underlined. N_p is the number of tuning parameters and t_t is the tuning time.

	RSC	RPC	ADC	RSAC	AIC	VI	PD
RMSE (rad)	0.0389	0.0333	0.0229	0.0268	<u>0.0218</u>	0.0804	0.0778
$E_{\max}$ (rad)	0.1938	0.0910	0.0923	0.0962	<u>0.0905</u>	0.2068	0.1931
$\tau_{\max}$ (N.m)	73	75	74	<u>72</u>	75	77	76
RMS_τ (N.m)	17.77	<u>15.90</u>	20.11	17.93	19.88	17.70	16.30
$\mathrm{N_p}$	24	18	28	36	28	9	<u>4</u>
$\mathrm{t_t}$ (min)	<u>5</u>	<u>5</u>	7	7	10	30	<u>5</u>

RSAC has the lowest $\tau_{\max}$, and the RPC has the best RMS_τ. However, the RSAC provides the best compromise between tracking performance and torque. From inspection of Table 5.1, the tuning process of all five model-based controllers is easier than the VI controller in spite of having only nine parameters, which is less than the number of the design parameters of the proposed controllers. Table 5.1 in general confirms that the proposed controllers outperform the VI and PD controllers regarding tracking performance and tuning, while providing a formal guarantee of stability and robustness in the presence of system uncertainties, unmodeled dynamics, and disturbances.

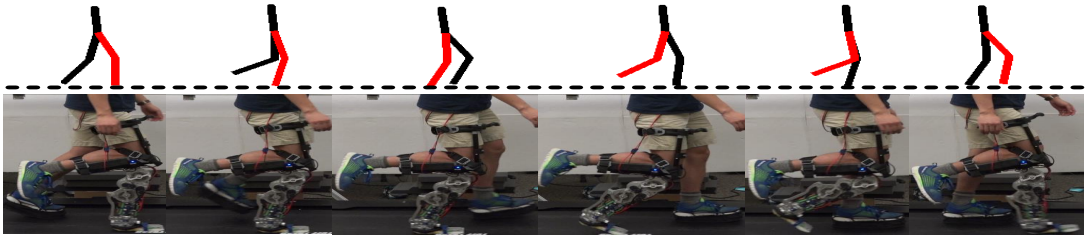

RSC

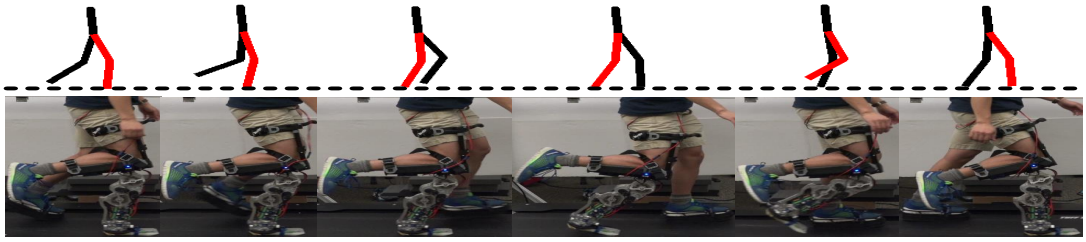

RPC

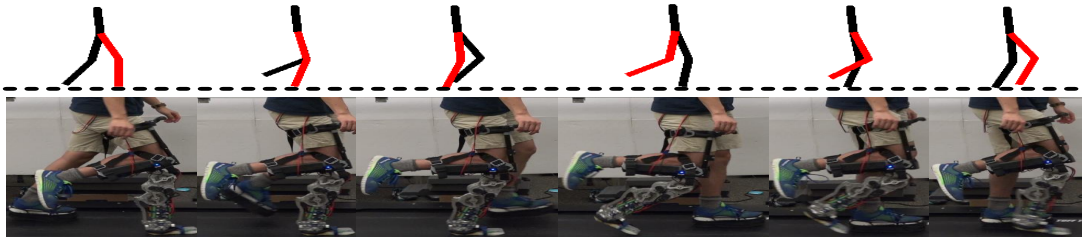

ADC

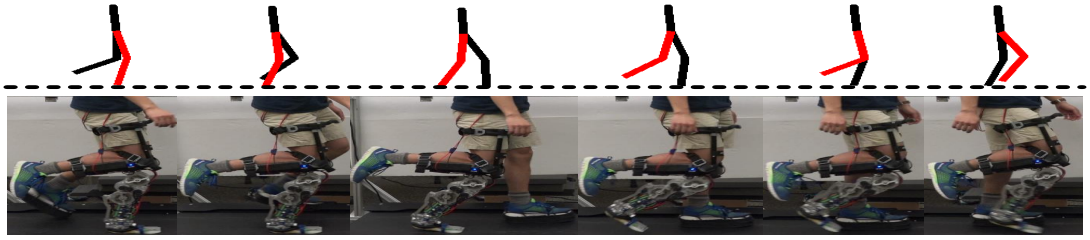

RSAC

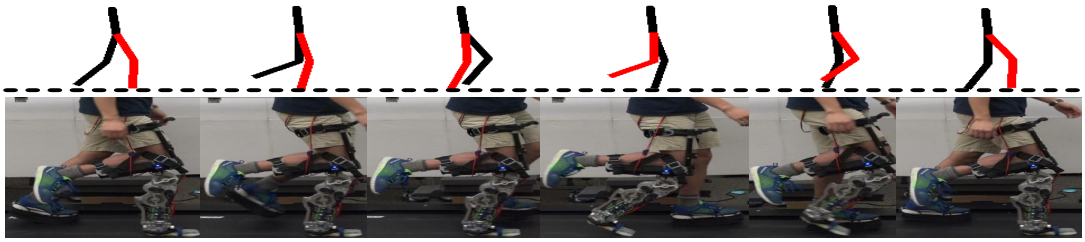

AIC

Figure 5.6: Gait tiles of human-prosthesis walking in simulation and AMPRO3 walking with an able-bodied human test subject in a treadmill test over two steps using all proposed controllers

5.5.3 Outdoor Test (Setup)

In addition to the treadmill test, an outdoor test is performed with AMPRO3 using the proposed controllers to verify their functionality in level ground and sloped walking. During the outdoor experiments, three able-bodied test subjects are asked to walk on level ground, uphill slopes, and downhill slopes for slope angles 3° and 8°, while wearing the prosthesis. The subjects are a 25-year-old female (Subject #1), a 28-year-old male (Subject #2), and a 22-year-old male (Subject #3). Subjects #1 and #2 performed the testing at California Institute of Technology (Caltech), and Subject #3 carried it out at Georgia Institute of Technology. The subjects wearing AMPRO3 are shown in Fig. 1.1. It should be pointed out that the level ground walking test is done with all subjects and the sloped walking test is carried out only at Caltech with Subjects #1 and #2. Based on the building codes in the United States, the maximum slope of a ramp shall be approximately 5° called *normal slope* [43]. The 3° and 8° slopes chosen in this work are regarded as a *mild slope* and an *extreme slope* respectively.

Remark 5: It should be noted that during the outdoor tests, the design parameters are unchanged and are the same as used in the treadmill test (Table 4.1). In other words, there is no need to adjust the controller parameters for different subjects, or for level and sloped walking. This shows that controllers are robust enough to deal with different users and different walking surfaces.

After testing, the subjects are asked to fill out a questionnaire to evaluate their satisfaction with the device: the prosthesis evaluation questionnaire (PEQ). The PEQ is categorized in four different groups (Group #1: Device satisfaction, Group #2: Bodily sensation, Group #3: Ability to move, and Group #4: Training satisfaction) to evaluate each subject's satisfaction and to indicate the functionality of prosthesis walking/quality of life. This questionnaire is a modified version of the PEQ [44] based on our experiments with AMPRO3 walking and healthy test subjects. The results of the questionnaire are given in Table 5.2.

The subjects also provided written feedback on each component of the survey. While the subjects are able to put the device on independently after some practice, they comment on the need

to have the straps of the iWalk adapter be very tight in order to feel confident in having a secure connection with the device. This leads to discomfort in the connected leg due to the tightness and rubbing of the straps when in contact with skin. However, the subjects do not experience much pain in their other leg or their back; the only noted pain is due to fatigue from extra work to compensate for the weight of the device and to ensure balance. One subject comments on the slight struggle to balance on the device with the extra weight and the shoe lift. Another subject mentions she had to control her balance in the frontal plane since the prosthesis is not actuated in this direction, but balance in the sagittal plane is satisfactory. The sound of the device does not bother one subject, but the other subjects comment on how this sound would be bothersome for daily use and a silent device would be preferred.

The subjects are moderately satisfied with their ability to walk with the device, although it takes practice to become accustomed to the extra mass, requiring extra attention to lift the device to prevent foot scuffing. This foot scuffing risk increases for walking up slopes, but is the only noted additional challenge for this terrain. For walking down slopes, one subject commented on the need to take smaller steps in order to feel stable due to the small, hard plastic foot which does not provide much grip on the ground or sense of security. Another subject notes that the device would sometimes not initiate a step when going down a slope. On the slopes, the ankle conforms nicely to the angle of the slope. All of the subjects are very satisfied with their training of the device and comment on the adequate time and support to adjust to the device and rest as needed.

5.5.4 Outdoor Test (Results)

During testing, data for the calculated desired position and velocity of the knee as well as the actual position and velocity of the knee are recorded, as measured by the on-board encoder. The actual knee torque is also calculated based on the current measured by the motor controllers. The subjects walk on flat ground for stretches of about 10 m. Figures 5.7 and 5.8 show tracking performance, phase portrait, and torque of the prosthetic knee for different subjects in outdoor level ground walking. It is observed that the proposed controller can accurately track the desired knee position

Table 5.2: Prosthesis evaluation questionnaire (PEQ) for three able-bodied subjects in the outdoor test. The questionnaire is categorized in four different groups as Group #1: Device satisfaction, Group #2: Bodily sensation, Group #3: Ability to move, and Group #4: Training satisfaction. Each subject (Subject #1, Subject #2, Subject #3) rates her/his satisfaction on a scale from 1 to 10 (1: Fully unsatisfied and 10 : Fully satisfied,) in different groups.

Question	Scale	Question	Scale
fitting[1]	(6,9,5)	sound[1]	(5,10,3)
weight[1]	(4,8,7)	pain in connected leg[2]	(4,8,2)
comfort while standing[1]	(6,5,8)	pain in other leg[2]	(7,9,8)
balance while using[1]	(7,7,5)	back pain[2]	(8,10,10)
socket comfortability[1]	(4,8,3)	ability to walk[3]	(6,8,7)
ease of wearing[1]	(8,7,6)	training to walk[4]	(9,10,9)
average of Group #1		(5.7,7.7,5.3)	
average of Group #2		(6.3,9,6.6)	
average of Group #3		(6,7,8)	
average of Group #4		(9,10,9)	

and provide convergence of the knee trajectory to a stable periodic orbit for all three subjects. According to Fig. 5.8, it can also be seen that the knee torques for different subjects have relatively similar magnitudes compared to the data from treadmill tests.

Subjects #1 and #2 walk up and down slopes of 3° and 8°, measured by a digital angle meter. These slopes are about 10.4 and 5.6 m long, respectively. All of the tests are performed outdoors on concrete sidewalks. At least 5 trials are done for each terrain type consisting of 10 strides or more. Figures 5.9 and 5.10 illustrate phase portraits of the prosthetic knee for different subjects in outdoor sloped walking for 3° and 8°. It is seen that the controller can provide stable limit cycles for the knee trajectories for different subjects walking on the mild and extreme slopes. This implies that the proposed controller is able to provide stable walking for uphill and downhill walking. Figure 5.11 shows gait tiles of outdoor AMPRO3 walking on level ground, uphill slopes, and downhill slopes for 3° and 8°. This figure shows that the proposed controller can provide qualitatively humanlike walking for subjects on level ground, and both uphill slopes and downhill slopes of 3° and 8°. Based on our experiments, sloped walking does not require higher torque at the knee than outdoor level ground and treadmill walking.

To visualize the performance of the proposed controllers, AMPRO3 walking results using the

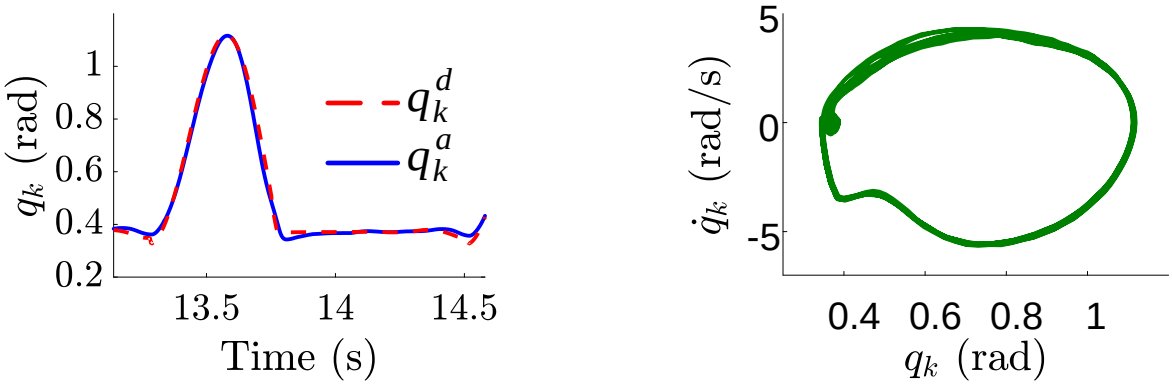

Subject #1

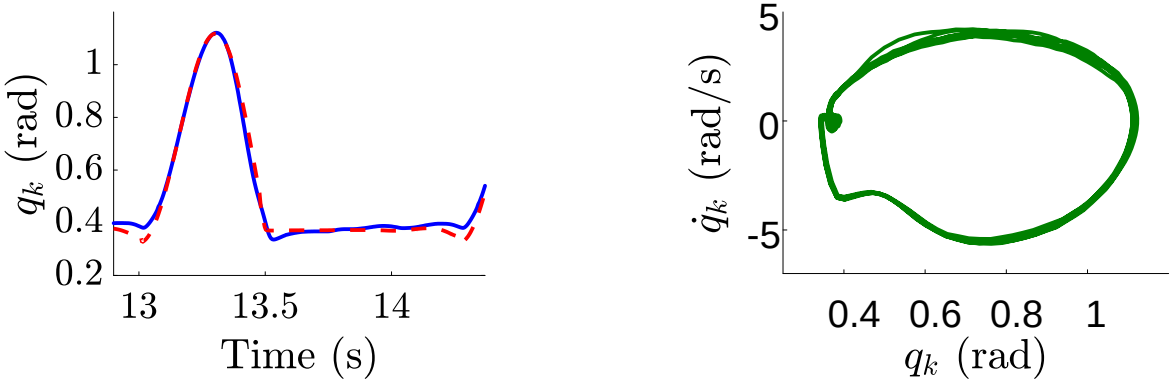

Subject #2

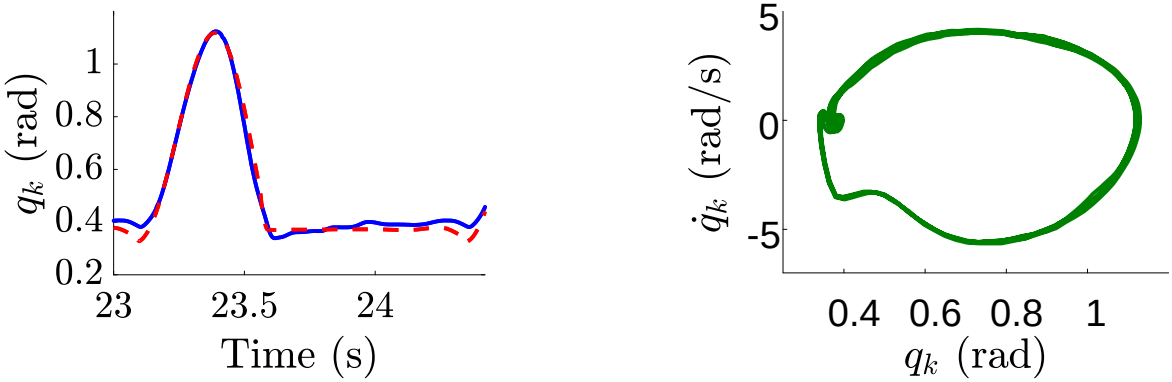

Subject #3

Figure 5.7: Tracking performance and phase portrait of the prosthetic knee for different subjects in outdoor level ground walking

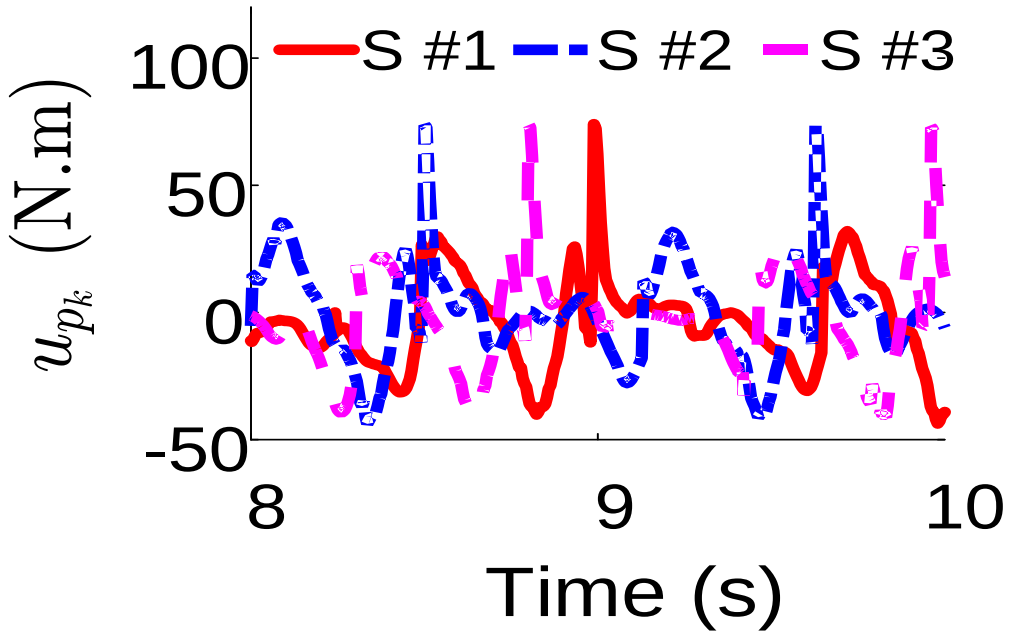

Figure 5.8: Torque of the prosthetic knee for different subjects in outdoor level ground walking (S #1: first subject, S #2: second subject, and S #3: third subject)

proposed controllers in simulation and experiments (treadmill and outdoor tests) can be seen in a video available at [24].

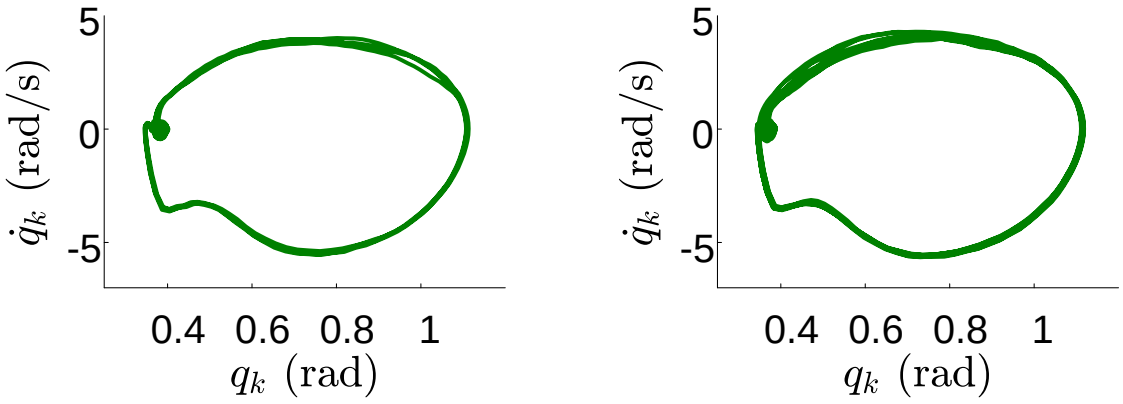

(a) Downslope walking 3°

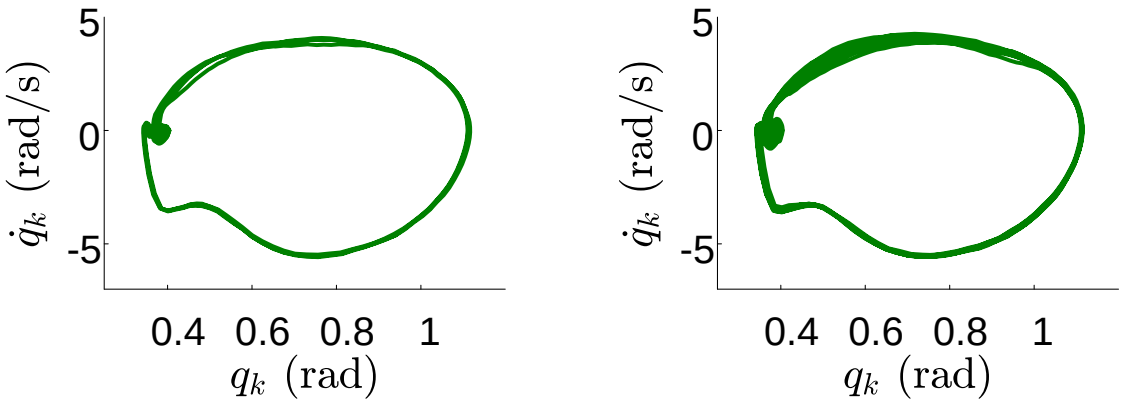

(b) Upslope walking 3°

Subject #1 Subject #2

Figure 5.9: Phase portraits of the prosthesis knee for different subjects in outdoor sloped walking of 3°

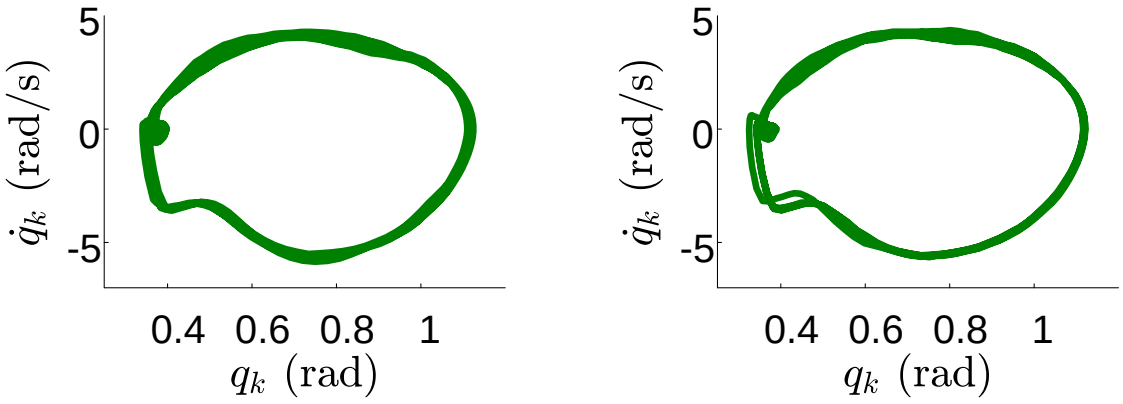

(a) Downslope walking 8°

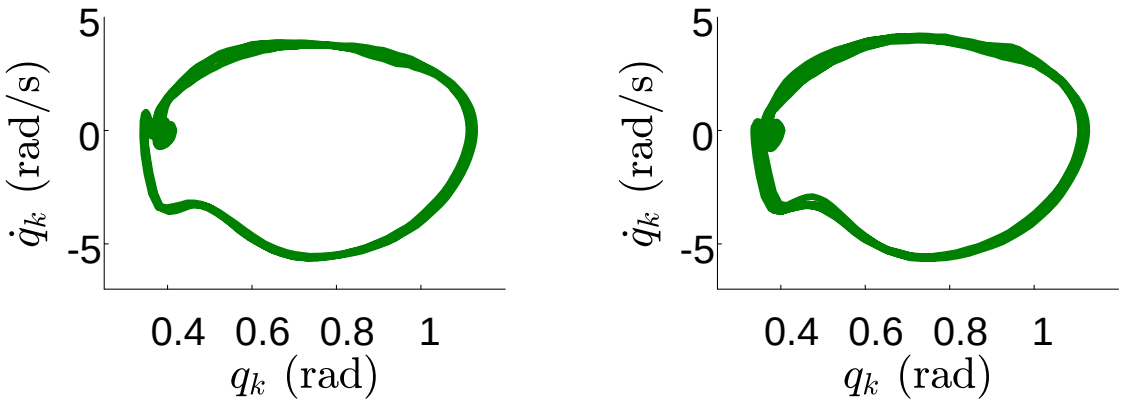

(b) Upslope walking 8°

Subject #1 Subject #2

Figure 5.10: Phase portraits of the prosthesis knee for different subjects in outdoor sloped walking of 8°

(a) Level ground walking

(b) Downhill walking 3°

(c) Uphill walking 3°

(d) Downhill walking 8°

(e) Uphill walking 8°

Figure 5.11: Gait tiles of outdoor AMPRO3 walking on level ground, uphill slopes, and downhill slopes of 3° and 8°

CHAPTER 6
CONCLUSION AND FUTURE WORK

The variable impedance and PD controllers are widely used for prosthetic leg control, wherein they have the advantage that they can be implemented in a model independent fashion. However, they are not amenable to formal stability analysis and do not provide proper tracking performance due to the presence of parameter uncertainties, unmodeled dynamics, and disturbances. This motivated the results presented in this work.

In this work, we designed and experimentally tested five different controllers to control a transfemoral prosthesis, addressing the above issues. The stability of all five controllers was proven using Lyapunov methods. This provides the first steps towards model-based adaptive and robust adaptive controllers to mitigate the disadvantages of the VI and PD controllers in that they give formal stability guarantees and, as shown in this thesis, improved performance. The proposed controllers were first verified on a walking biped platform and then successfully implemented on AMPRO3.

Simulation results showed that all proposed controllers provided good prosthetic knee tracking performance and humanlike walking. Their results were compared against each other. The RSC provided the best robustness and stability in the presence of disturbances, the AIC provided the best tracking performance, and the RSAC provided the best compromise between these objectives.

All proposed model-based controllers were experimentally verified on AMPRO3 using able-bodied test subjects on a treadmill and compared with VI and PD controllers. Treadmill results showed that all newly proposed controllers outperformed both VI and PD controllers in tracking and parameter tuning time. In addition to the treadmill test, an outdoor test was performed using AMPRO3 with three able-bodied test subjects walking on level ground, uphill slopes, and downhill slopes of 3° and 8°. The outdoor tests revealed that the proposed approaches were able to provide human-like and stable walking for AMPRO3 on different uneven surfaces.

The content of this thesis is IEEE-copyrighted, and was published in the *IEEE Transactions on Systems, Man and Cybernetics: Systems* [45] and the *American Control Conference* [37].

Future work would aim to consider the following tasks:

1. In this work, the robustness test was only performed in simulation for the biped model. However, additional experiments can be performed to quantify robustness to unexpected pushes and obstacles using the proposed controllers.

2. The effect of ground reaction force (GRF) was not considered, so an observer/controller combination can be designed for the biped platform in simulation, and then experimentally implemented on AMPRO3 to provide GRF estimation-based control.

3. This work presented different model-based controllers for AMPRO3 while the ankle joint was assumed to be passive. However, a powered ankle is able to provide positive net work and power during the stance phase while walking at moderate to fast walking speeds [46, 47]. Thus, modifying the proposed controllers to include both knee and ankle could reduce the metabolic energy cost of walking, in turn enhancing the quality of gait.

4. This work validated the soundness of model-based controllers for walking on level ground and ramps. However, stair ascent and descent remain interesting problems that could be addressed in future work with extensions of the proposed controllers. These controllers along with stable human-like gait generation could provide a stair ascent and descent control system for a powered knee and ankle prosthesis to further empower amputees in their daily life.

REFERENCES

[1] T. Dillingham *et al.*, "Limb amputation and limb deficiency: Epidemiology and recent trends in the United States," *Southern Medical Journal*, vol. 95, no. 8, pp. 875–884, 2002.

[2] Z. W. Lui, M. I. Awad, A. Abouhossein, A. A. Dehghani-Sanij, and N. Messenger, "Virtual prototyping of a semi-active transfemoral prosthetic leg," *Proceedings of the Institution of Mechanical Engineers, Part H: Journal of Engineering in Medicine*, vol. 229, no. 5, pp. 350–361, 2015.

[3] F. Sup, H. A. Varol, and M. Goldfarb, "Upslope walking with a powered knee and ankle prosthesis: Initial results with an amputee subject," *IEEE Transactions on Neural Systems and Rehabilitation Engineering*, vol. 19, no. 1, pp. 71–78, 2011.

[4] D. A. Winter, *The Biomechanics and Motor Control of Human Gait: Normal, Elderly, and Pathological*. University of Waterloo Press, 1991.

[5] B. E. Lawson, H. A. Varol, and M. Goldfarb, "Standing stability enhancement with an intelligent powered transfemoral prosthesis," *IEEE Transactions on Biomedical Engineering*, vol. 58, no. 9, pp. 2617–2624, 2011.

[6] A. M. Simon, K. A. Ingraham, J. A. Spanias, A. J. Young, S. B. Finucane, E. G. Halsne, and L. J. Hargrove, "Delaying ambulation mode transition decisions improves accuracy of a flexible control system for powered knee-ankle prosthesis," *IEEE Transactions on Neural Systems and Rehabilitation Engineering*, vol. 25, no. 8, pp. 1164–1171, 2017.

[7] F. Sup, A. Bohara, and M. Goldfarb, "Design and control of a powered transfemoral prosthesis," *International Journal of Robotics Research*, vol. 27, no. 2, pp. 263–273, 2008.

[8] N. Fey, A. Simon, A. Young, and L. Hargrove, "Controlling knee swing initiation and ankle plantarflexion with an active prosthesis on level and inclined surfaces at variable walking speeds," *IEEE Journal of Translational Engineering in Health and Medicine*, vol. 2, pp. 1–12, 2014.

[9] C. G. Atkeson and S. Schaal, "Robot learning from demonstration," *International Conference on Machine Learning*, vol. 97, pp. 12–20, 1997.

[10] H. Zhao, J. Horn, J. Reher, V. Paredes, and A. D. Ames, "First steps toward translating robotic walking to prostheses: A nonlinear optimization based control approach," *Autonomous Robots*, vol. 19, no. 1, pp. 1–18, 2011.

[11] H. Zhao and et al., "Multicontact locomotion on transfemoral prostheses via hybrid system models and optimization-based control," *IEEE Transactions on Automation Science and Engineering*, vol. 13, no. 2, pp. 502–513, 2016.

[12] Y. Wen, J. Si, X. Gao, S. Huang, and H. H. Huang, "A new powered lower limb prosthesis control framework based on adaptive dynamic programming," *IEEE Transactions on Neural Networks and Learning Systems*, vol. 28, no. 9, pp. 2215–2220, 2017.

[13] F. Ferraguti, C. Secchi, and C. Fantuzzi, "A tank-based approach to impedance control with variable stiffness," in *IEEE International Conference on Robotics and Automation*, Karlsruhe, Germany, 2013.

[14] K. Kronander and A. Billard, "Stability considerations for variable impedance control," *IEEE Transactions on Robotics*, vol. 32, no. 5, pp. 1298–1305, 2016.

[15] W. He, W. Ge, Y. Li, Y. Liu, C. Yang, and C. Sun, "Model identification and control design for a humanoid robot," *IEEE Transactions on Systems, Man, and Cybernetics: Systems*, vol. 47, no. 1, pp. 45–57, 2017.

[16] M. Van, M. Mavrovouniotis, and S. S. Ge, "An adaptive backstepping nonsingular fast terminal sliding mode control for robust fault tolerant control of robot manipulators," *IEEE Transactions on Systems, Man, and Cybernetics: Systems*, pp. 1–11, 2018.

[17] J. Yao and W. Deng, "Active disturbance rejection adaptive control of uncertain nonlinear systems: Theory and application," *Nonlinear Dynamics*, vol. 89, no. 3, pp. 1611–1624, 2017.

[18] W. Deng and J. Yao, "Adaptive integral robust control and application to electromechanical servo systems," *ISA Transactions*, vol. 67, pp. 256 –265, 2017.

[19] V. Azimi, T. T. Nguyen, M. Sharifi, S. A. Fakoorian, and D. Simon, "Robust ground reaction force estimation and control of lower-limb prostheses: Theory and simulation," *IEEE Transactions on Systems, Man, and Cybernetics: Systems*, pp. 1–12, 2018.

[20] H. Ma, Z. Wang, D. Wang, D. Liu, P. Yan, and Q. Wei, "Neural-network-based distributed adaptive robust control for a class of nonlinear multiagent systems with time delays and external noises," *IEEE Transactions on Systems, Man, and Cybernetics: Systems*, vol. 46, no. 6, pp. 750–758, 2016.

[21] C. Sun, W. He, W. Ge, and C. Chang, "Adaptive neural network control of biped robots," *IEEE Transactions on Systems, Man, and Cybernetics: Systems*, vol. 47, no. 2, pp. 315–326, 2017.

[22] L. Ding, S. Li, Y. Liu, H. Gao, C. Chen, and Z. Deng, "Adaptive neural network-based tracking control for full-state constrained wheeled mobile robotic system," *IEEE Transactions on Systems, Man, and Cybernetics: Systems*, vol. 47, no. 8, pp. 2410–2419, 2017.

[23] R. Cui, C. Yang, Y. Li, and S. Sharma, "Adaptive neural network control of auvs with control input nonlinearities using reinforcement learning," *IEEE Transactions on Systems, Man, and Cybernetics: Systems*, vol. 47, no. 6, pp. 1019–1029, 2017.

[24] V. Azimi, "Experimental and simulation results of AMPRO3 walking," `https://youtu.be/7tNctFvII5o`, accessed November 20, 2018.

[25] E. R. Westervelt, J. W. Grizzle, C. Chevallereau, J. H. Choi, and B. Morris, *Feedback Control of Dynamic Bipedal Robot Locomotion*. Boca Raton: CRC Press, 2007.

[26] A. D. Ames, "First steps toward automatically generating bipedal robotic walking from human data," *Robotic Motion and Control*, vol. 422, 2011.

[27] M. Spong, S. Hutchinson, and M. Vidyasagar, *Robot Modeling and Control*. Wiley, 2005.

[28] Y. Hurmuzlu and D. B. Marghitu, "Rigid body collisions of planar kinematic chains with multiple contact points," *International Journal of Robotics Research*, vol. 13, no. 1, pp. 82–92, 1994.

[29] E. Westervelt, J. Grizzle, and D. E. Koditschek, "Hybrid zero dynamics of planar biped walkers," *IEEE Transactions on Automatic Control*, vol. 48, no. 1, pp. 42–56, 2003.

[30] A. D. Ames, "Human-inspired control of bipedal walking robots," *IEEE Transactions on Automatic Control*, vol. 59, no. 5, pp. 1115–1130, 2014.

[31] H. Zhao, "From bipedal locomotion to prosthetic walking: A hybrid system and nonlinear control approach," PhD thesis, Georgia Institute of Technology, 2016.

[32] H. Zhao, M. Powell, and A. D. Ames, "Human-inspired motion primitives and transitions for bipedal robotic locomotion in diverse terrain," *Optimal Control Applications and Methods*, vol. 35, no. 6, 730–755, 2013.

[33] A. D. Ames, K. Galloway, K. Sreenath, and J. W. Grizzle, "Rapidly exponentially stabilizing control lyapunov functions and hybrid zero dynamics," *IEEE Transactions on Automatic Control*, vol. 59, no. 4, pp. 876–891, 2014.

[34] J.-J. E. Slotine and W. Li, "Adaptive manipulator control: A study case," *IEEE Transactions on Automatic Control*, vol. 33, no. 11, pp. 995–1003, 1988.

[35] J. J. Slotine and W. Li, *Applied Nonlinear Control*. Prentice-Hall, 1991.

[36] J.-J. E. Slotine and J. A. Coetsee, "Adaptive sliding controller synthesis for non-linear systems," *International Journal of Control*, vol. 43, no. 6, pp. 1631–1651, 1984.

[37] V. Azimi, T. Shu, H. Zhao, E. Ambrose, A. D. Ames, and D. Simon, "Robust control of a powered transfemoral prosthesis device with experimental verification," in *Proceedings of the American Control Conference*, Seattle, WA, 2017.

[38] V. Azimi, D. Simon, and H. Richter, "Stable robust adaptive impedance control of a prosthetic leg," in *Proceedings of the ASME Dynamic Systems and Control Conference*, Columbus, OH, 2015.

[39] V. Azimi, D. Simon, H. Richter, and S. A. Fakoorian, "Robust composite adaptive transfemoral prosthesis control with non-scalar boundary layer trajectories," in *Proceedings of the American Control Conference*, Boston, MA, 2016.

[40] H. Zhao, E. Ambrose, and A. D. Ames, "Preliminary results on energy efficient 3D prosthetic walking with a powered compliant transfemoral prosthesis," in *IEEE International Conference on Robotics and Automation*, Singapore, 2017.

[41] P. W. Duncan, D. K. Weiner, J. Chandler, and S. Studenski, "Functional reach: A new clinical measure of balance," *Journal of Gerontology*, vol. 45, no. 6, M192M197, 1990.

[42] D. Brooks, J. Parsons, J. P. Hunter, M. Devlin, and J. Walker, "The 2-minute walk test as a measure of functional improvement in persons with lower limb amputation," *Archives of Physical Medicine and Rehabilitation*, vol. 82, no. 10, pp. 1478 –1483, 2001.

[43] F. Sup, H. A. Varol, and M. Goldfarb, "Upslope walking with a powered knee and ankle prosthesis: Initial results with an amputee subject," *IEEE Transactions on Neural Systems and Rehabilitation Engineering*, vol. 19, no. 1, pp. 71–78, 2011.

[44] "Prosthesis evaluation questionnaire," in *Prosthetics Research Study*, Seattle, WA, 1998.

[45] V. Azimi, T. Shu, H. Zhao, R. Gehlhar, D. Simon, and A. D. Ames, "Model-based adaptive control of transfemoral prostheses: Theory, simulation, and experiments," *IEEE Transactions on Systems, Man, and Cybernetics: Systems*, pp. 1–18, 2019.

[46] A. Hansen, D. Childress, S. Miff, S. Gard, and K. Mesplay, "The human ankle during walking: Implication for the design of biomimetric ankle prosthesis," *J. Biomech.*, vol. 37, no. 10, 14671474, 2004.

[47] S. K. Au, J. Weber, and H. Herr, "Powered ankle–foot prosthesis improves walking metabolic economy," *IEEE Transactions on Robotics*, vol. 25, no. 1, pp. 51–66, 2009.